

Improving AUV Localization Accuracy by Combining Ultra-Short-Baseline and Long-Baseline Measurement Systems in a Post-Processing Extended Kalman Filter

A Thesis

Presented in Partial Fulfillment of the Requirements for the

Degree of Master of Science

with a

Major in Mechanical Engineering

in the

College of Graduate Studies

University of Idaho

by

David Halverson Pick II

Major Professor: Eric Wolbrecht, Ph.D.

Committee Members: Michael Anderson, Ph.D.; Dean Edwards, Ph.D.

Department Administrator: Steven Beyerlein, Ph.D.

May 2019

Abstract

The University of Idaho (UI), partnered with the Office of Naval Research (ONR), is developing the capability to perform oceanographic survey measurements conducted by autonomous underwater vehicles (AUVs). Accurate spatial and temporal localization of these measurements is essential to properly correlate electric and magnetic field measurements to the desired reference frame. Previous work at UI has investigated the use of long baseline (LBL), moving short baseline (MSBL), and hybrid baseline (HBL) for navigation and localization. LBL navigation systems can have a high degree of accuracy but have a limited operating range and are not easily re-deployed and surveyed. Field testing operations at the University of Idaho continue to expand, including consideration of ultra-short baseline (USBL) localization and navigation as an alternative or augmentation to existing LBL navigation systems due to advantages in deployability. The acoustic ranging from these systems are used in an extended Kalman filter (EKF) to estimate orientation and position. This information is utilized by the AUV to navigate along a waypoint course and stored in a log for post-process analysis and further study.

This paper presents a series of Monte Carlo simulations that were performed to compare the measurement uncertainty between conventional LBL and USBL systems. The simulated North and East position measurements from the USBL were used as additional measurements in a new post-processing EKF. This was performed in several different cases, allowing for the comparison between the legacy EKF and differing variants of a post-processing EKF using USBL measurements. Each of these simulations utilized historic UI field testing LBL range and AUV sensor measurements in addition to simulated USBL measurements.

Results from Monte Carlo simulations suggest that USBL localization uncertainty is better than that of LBL, albeit for a smaller operating range. This smaller operating range comes from poor depth uncertainty and a lack of depth telemetry. Additionally, it was found that the addition of USBL measurements to the existing EKF greatly improved the state estimate uncertainty for AUV position over the legacy EKF. USBL systems often provide a telemetry-based depth measurement, which communicates depth from the AUV to the USBL transceiver and greatly improves the uncertainty of the USBL system. When depth telemetry

is implemented, the USBL has a lower uncertainty than the EKF does, but the EKF provides additional confidence in the state estimates due to the combination of independent measurement systems and the addition of the AUV kinematic model.

Acknowledgements

I would like to thank my major professor, Dr. Wolbrecht, who has been an immense help through the course of my research. Additionally, I would like to thank Dr. Anderson, who has been a phenomenal resource and helped me expand my horizons throughout my graduate degree. Also, I would like to thank all those who have worked on the project, past and present, who have laid a strong foundation to build from.

Dedication

I am so thankful for my family for all the support they've provided throughout my Master's degree. My wife, Merrill-Lee, for her love, compassion, and the occasional correction, I am eternally grateful. My parents, for supporting my decision to pursue a Master's and help in any way they could. My mother and father-in-law, for being my second set of cheerleaders. Also, my homegroup family from church who have supported Merrill-Lee and I throughout the past few years, they provided so much love, wisdom, and prayers that helped us carry through. Most importantly, I am so thankful for my Lord, Jesus Christ, who is constantly shaping me to be the man I can be, one who has a heart after His.

Table of Contents

| | |
|--|-----|
| Authorization to Submit Thesis | ii |
| Abstract | iii |
| Acknowledgements | v |
| Dedication | vi |
| Table of Contents | vii |
| List of Figures | ix |
| List of Tables | x |
| Chapter 1: Introduction | 1 |
| 1.1. Project Background | 1 |
| 1.2. Ultra-Short-Baseline Navigation | 1 |
| 1.3. Combining Ultra-Short and Long Baseline Systems | 2 |
| 1.4. Extended Kalman Filter Monte Carlo Integration | 3 |
| Chapter 2: Methods | 5 |
| 2.1 University of Idaho AUVs | 5 |
| 2.2 Field Testing | 6 |
| 2.3 Ultra-Short Baseline Localization | 6 |
| 2.3.1 Ultra-Short Baseline System Geometry | 6 |
| 2.3.2 USBL System Orientation | 8 |
| 2.3.3 USBL in Global Reference Frame | 9 |
| 2.4 Monte Carlo Simulation | 10 |
| 2.4.1 USBL Configurations for Monte Carlo Simulations | 10 |
| 2.4.2 Ship Referenced Monte Carlo Simulation and Modeled Uncertainty | 11 |
| 2.4.3 Geo-Referenced USBL Uncertainty Monte Carlo | 14 |
| 2.5 Extended Kalman Filter | 16 |

| | | |
|--|---|----|
| 2.6 | Depth Estimation EKF | 18 |
| 2.6.1 | Legacy EKF and Case 1: Post-Process EKF..... | 19 |
| 2.6.2 | Case 2: Post-Process EKF plus USBL North and East Measurements | 21 |
| 2.6.3 | Case 3: Post-Process EKF plus AUV Depth..... | 21 |
| 2.6.4 | Case 4: Post-Process EKF plus USBL North, East, and Depth Measurements | 22 |
| 2.6.5 | Case 5: Post-Process EKF plus AUV Depth, USBL North and East Measurements, and USBL Telemetry Depth Measurements..... | 23 |
| 2.7 | EKF Covariance Matrices | 24 |
| 2.7.1 | Process Noise Covariance Matrix | 24 |
| 2.7.2 | Measurement Noise Covariance Matrix | 26 |
| 2.7.3 | State Covariance Matrix | 29 |
| Chapter 3: Results and Discussion..... | | 32 |
| 3.1. | USBL Monte Carlo Simulation Results | 32 |
| 3.1.1. | Results in Transceiver Reference Frame | 32 |
| 3.1.2. | Results in Global Reference Frame | 37 |
| 3.1.3. | Summary of USBL Uncertainty Results..... | 42 |
| 3.2. | EKF Results..... | 42 |
| Chapter 4: Conclusions | | 48 |
| 4.1. | USBL Integration | 48 |
| 4.1.1. | USBL Monte Carlo Studies | 48 |
| 4.1.2. | USBL-EKF Integration..... | 49 |
| 4.2. | Future Work | 50 |
| 4.2.1. | Field Testing | 50 |
| 4.2.2. | Rauch-Tung-Striebel Smoother | 50 |
| References..... | | 51 |

List of Figures

| | | |
|-----|--|----|
| 2.1 | UI AUV equipped with electric field probe and additional sensor array | 5 |
| 2.2 | Ship-mounted USBL system geometry tracking an AUV | 7 |
| 2.3 | Tilt angle, α , of the USBL transceiver about the North axis of the transceiver reference frame | 9 |
| 2.4 | Fixed-depth (top) and fixed-north (bottom) analysis planes during USBL Monte Carlo simulations | 11 |
| 2.5 | Measurement noise model for depression and heading angles | 13 |
| 3.1 | Measurement uncertainty heatmaps for LBL Monte Carlo simulation | 32 |
| 3.2 | Measurement uncertainty heatmaps for $N=0$ fixed-north USBL tilt configurations ... | 34 |
| 3.3 | Measurement uncertainty heatmaps for components of $N=0$ fixed-north USBL..... | 35 |
| 3.4 | Measurement uncertainty heatmaps for $D=10$ fixed-depth USBL configurations..... | 36 |
| 3.5 | Measurement uncertainty heatmaps for $N=0$ fixed-north USBL configurations with ship orientation uncertainties | 38 |
| 3.6 | Measurement uncertainty heatmaps for $N=0$ fixed-north USBL configurations with ship orientation and GPS uncertainties | 39 |
| 3.7 | Measurement uncertainty heatmaps for $N=0$ fixed-north USBL configurations with ship orientation uncertainties: High accuracy instrumentation..... | 41 |
| 3.8 | EKF simulation results..... | 46 |
| 3.9 | EKF simulation results, zoomed..... | 47 |

List of Tables

| | | |
|-----|---|----|
| 2.1 | Process Noise Covariance Values..... | 26 |
| 2.2 | Measurement Noise Covariance Values | 29 |
| 2.3 | Initial State Covariance Values..... | 31 |

Chapter 1: Introduction

Portions of this paper appear in “Uncertainty Analysis of Ultra-Short- and Long-Baseline Localization Systems for Autonomous Underwater Vehicles”, published in: Proceedings of the IEEE/MTS OCEANS Conference, Charlotte, 22-25 Oct. 2018.

1.1. Project Background

The US Navy Office of Naval Research (ONR) has partnered with researchers at the University of Idaho (UI) to develop capabilities to perform and analyze electric and magnetic field measurements in underwater ocean environments. Currently, a fleet of autonomous underwater vehicles (AUVs), equipped with electric and magnetic field sensors, are being used in field testing to perform the surveys. Accurate spatial and temporal localization of each AUV is critically important to properly correlate electric and magnetic field data to the desired reference frame. This accuracy depends on the type, quantity, and configuration of the localization hardware.

Currently, the UI fleet of AUVs utilizes long-baseline (LBL) navigation systems with four to five acoustic transponders to perform AUV navigation and localization. The AUVs use an extended Kalman filter (EKF) to estimate their position and orientation, with acoustic ranges determined from two-way travel time to each LBL transponder in the array [1]–[3]. LBL systems are capable of a high degree of accuracy over the testing range, typically within a meter (for a review of AUV localization and navigation techniques, see [4]–[6]). These LBL arrays can either be fixed to permanent seafloor anchors or deployed and surveyed prior to testing. Permanently moored transponders create a stable testing range but may not be allowed in all desired measurement locations. Temporary deployments are more flexible but require additional time prior to testing for surveying to determine transponder locations accurately.

1.2. Ultra-Short-Baseline Navigation

Ultra-short-baseline (USBL) localization and navigation is currently under consideration as an alternative or augmentation to existing LBL navigation systems due to

advantages in deployability ([4]–[6]). These systems may be mounted on a surface ship allowing for AUV localization in forward locations with less time investment in measurement range preparation. Commercial USBL systems have typical range accuracy between 0.5 and 3% of the slant range between the surface transceiver and the target transponder (see [7] for a discussion of error sources). Since the accuracy is range dependent, the placement of the surface ship relative to the AUV during mission navigation is highly important. The USBL positioning can be further improved using differential global positioning systems (DGPS) and/or real-time kinetic (RTK) systems mounted to the surface ship. The DGPS or RTK systems reduces the positional uncertainty of the USBL transceiver in the global reference frame, thus improving the AUV position estimate uncertainty.

In order to make the desired oceanographic measurements, localization accuracy at least as good as an LBL system is required. Previous work has evaluated AUV navigation and localization techniques, including USBL and LBL systems [4]. Localization accuracy is always an important consideration, and has been studied for LBL systems [8] and others, although many factors contribute to the choice of localization system. An alternative approach is to combine systems to improve localization accuracy [9]–[12].

The current UI research is focused on improving AUV localization during field tests, therefore USBL navigation and localization is under investigation. USBL is known to have spatial accuracy dependence, e.g., the system accuracy is typically presented as a percentage of slant range; therefore, an uncertainty analysis must be performed to compare USBL to current LBL systems implemented by UI. The uncertainties present in the USBL are assumed to be Gaussian, but due to the form of the nonlinear equations describing the spatial dependency of the USBL accuracy, it would be challenging to implement USBL measurements directly within the existing UI AUV EKF. Therefore, a Monte Carlo analysis of USBL tracking performance was performed to quantify the spatial dependence of USBL systems. This was followed by an investigation into implementing a depth state and USBL measurements into a post-processing EKF.

1.3 Combining Ultra-Short and Long Baseline Systems

Previous work has investigated the combination of USBL and LBL systems [9]–[12]. Each of these research teams utilized a USBL transceiver mounted to an AUV to

communicate with an LBL array. The work in [9]-[12] does not utilize USBL and LBL as independent measurements of AUV position. In [12], the combined system was evaluated experimentally, utilizing surface missions to determine the LBL moored modem locations and then performing underwater missions, navigating based on acoustic ranging. The measurements in [12] were utilized in an Extended Kalman Filter (EKF) and additional post-processing through a smoothing filter improved position results. The measurement error reported in [12] was $3\text{-}23m$. This is significantly greater uncertainty than is acceptable for the UI AUV localization applications. The work presented in [9]-[11] performed simulation testing of the combined USBL/LBL system, achieving a globally exponentially stable navigation system in [9] and [10] and a globally asymptotically stable navigation system in [11]. The researchers in [9]-[11] utilized a Kalman filter rather than an EKF and reported position error bounds of less than $1m$ in [10]. In [11], the standard deviation of the steady-state estimation error was found to be less than $0.4m$ when averaged over 1000 Monte Carlo simulations. The USBL can determine its position from a single LBL reply; therefore, the addition of multiple LBL beacons increases the amount of information available to determine AUV position.

The work presented in this paper presents a novel approach to the combination of USBL and LBL navigation systems. Rather than utilizing a USBL receiver to communicate with an LBL moored transponder array, this work proposes the combination of two separate acoustic systems, each measuring AUV location independently. The measurements from these systems, LBL and USBL, are integrated in an EKF in simulation, utilizing field testing LBL measurements as a baseline for comparison of the simulated systems. The results presented will provide data for future equipment requisitions. Additionally, the use of depth telemetry data from a USBL beacon will be considered to improve the uncertainty of the USBL depth measurement.

1.4 Extended Kalman Filter Monte Carlo Integration

Measurement uncertainty of USBL systems is spatially dependent; therefore, the measurement noise implemented within the EKF is state-dependent. The methodology proposed in this paper utilizes Monte Carlo methods to implement the spatially varying measurement noise. Previous work has investigated the use of Monte Carlo methods to

augment a Kalman filter [13]. The researchers in [13] propose a Monte Carlo Kalman Filter (MCKF) as a simple, computationally inexpensive method of handling nonlinear state space models with non-normal distributions. This methodology, to the best of the author's knowledge, has only been applied to unmanned aerial vehicles (UAVs) [14].

The methodology presented in this paper presents a novel approach to combining an EKF and Monte Carlo methods. The Monte Carlo simulation is utilized to determine the USBL measurement uncertainty at the current AUV position. Due to the spatial dependence of USBL uncertainty, the USBL measurement uncertainty determined by the Monte Carlo simulation is used to seed the measurement uncertainty applied within the EKF. This expands upon previous work at UI [15], where the measurement noise implemented within the EKF was not state-dependent.

Chapter 2: Methods

2.1 University of Idaho AUVs

The University of Idaho AUV is based on the Virginia Polytechnic Institute AUV [16]. The AUVs are approximately 1m in length and 10cm in diameter, which allows a single person to deploy them in the field. Further details regarding the UI AUV design can be found in [17].



Figure 2.1: UI AUV Equipped with electric field probe and additional sensor array.

The AUVs are equipped with various sensors and hardware to enable navigation, communication, and other necessary processes. These include: a Woods Hole Oceanographic Institute (WHOI) micro-modem used for acoustic communication and LBL navigation pings; a capacitive pressure transducer to measure AUV depth; a GPS unit and mast to provide localization information during surface operation; an inertial measurement unit (IMU) to measure angular rates of change and linear accelerations; and a radio antenna to provide remote operation and real-time telemetry data. More detail regarding the on-board sensors can be found in [18].

The UI AUVs have previously been used to conduct fleet operations [19], magnetic signature measurements [20],[21], and oceanographic electric field measurements [22],[23]. Figure 2.1 shows an electric field probe and sensor container to hold a standalone sensor system attached to the bottom of the AUV. This configuration of the AUV allows for the collection of both electric and magnetic field measurements simultaneously with a single AUV. As research progresses and oceanographic measurement capabilities expand, it is desired to improve the localization of the AUV position.

2.2 Field Testing

The Acoustic Research Detachment (ARD) of the Naval Surface Warfare Center, Carderock Division, has a field testing facility located on Lake Pend Oreille in Bayview, Idaho. This location includes two long baseline (LBL) test ranges, one in-bay which allows AUVs to operate at 3 meters below the water line and a second near a fixed barge that allows AUV mission depths up to 50 meters. This testing range is near to UI, allowing for frequent field testing.

2.3 Ultra-Short Baseline Localization

2.3.1 Ultra-Short Baseline System Geometry

Ultra-short baseline (USBL) acoustic tracking systems are being considered as an alternative to current localization methods in use at UI. A typical mission implementation uses a USBL transceiver mounted to a surface ship to track an AUV (see Figure 2.2). The objective is to determine the AUV position relative to the USBL transceiver mounted to the surface ship. In Figure 2.2, the top horizontal plane shown is the plane parallel and coincident to the USBL transceiver head. USBL systems typically are mounted either to the bottom of the surface ship or attached to a rigging that holds the transceiver approximately one meter below the bottom of the ship to prevent acoustic reception interference from the ship's hull.

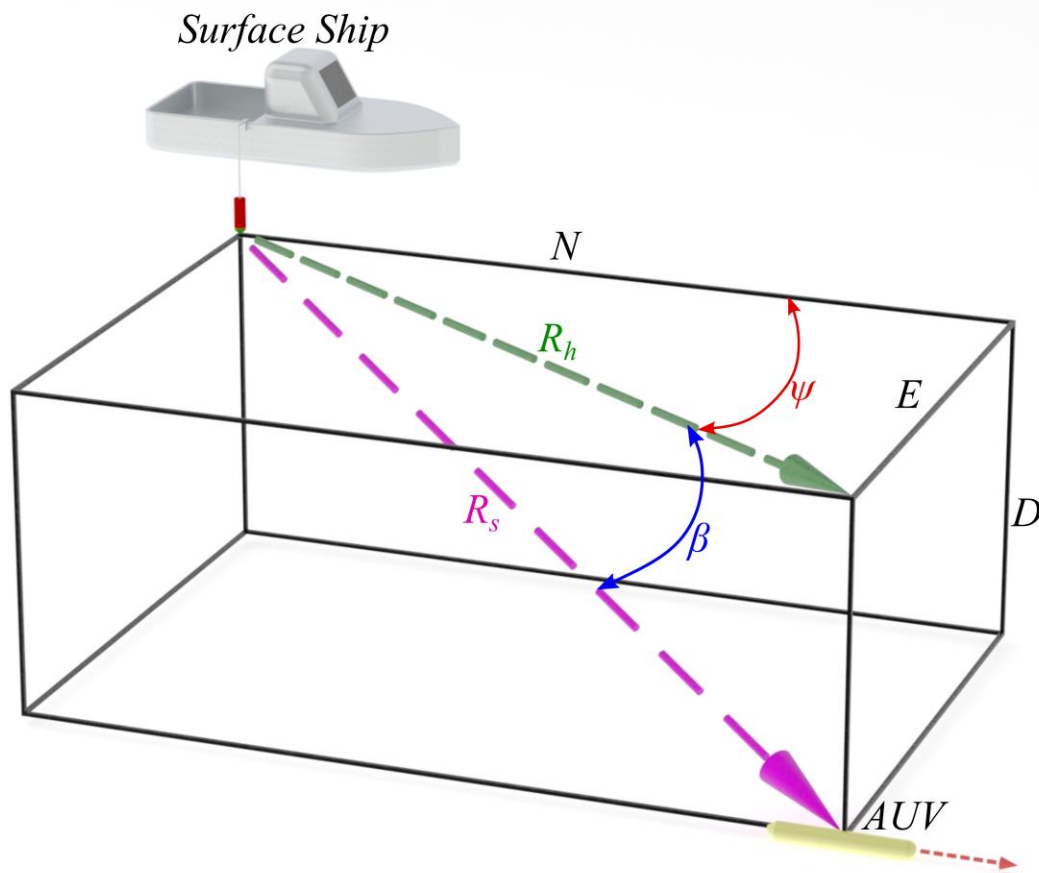


Figure 2.2: Ship-mounted USBL system tracking an AUV. The USBL system directly measures slant range, R_s , depression angle, β , and heading angle, ψ . These variables are used to calculate heading range, R_h , and then the AUV positions North, N , East, E , and depth, D .

The analysis performed presumes a typical USBL system that measures the direct path slant range, R_s , between the transceiver on the surface ship and the transponder on the AUV. The USBL system also measures the depression angle, β , of the slant range, and the heading angle, ψ , of the AUV position relative to the orientation of the transceiver on the surface ship. These three measurements are then used to calculate the horizontal range, R_h , and the coordinates of the AUV, where N is the North position E is the East position, and D is the depth.

The USBL system calculates slant range, R_s , as:

$$R_s = \left(\frac{t - t_0}{2} \right) c ; \quad (2.1)$$

where t is the total two-way travel time (TWTT) of acoustic communication between the transceiver and the target, t_0 , is the fixed electronic system turnaround time, and c is the absolute speed of sound in water.

Horizontal range, R_h , is the slant range projected onto the horizontal plane of the USBL transceiver (parallel to the water surface plane when the transceiver is mounted vertically). It is calculated according to:

$$R_h = R_s \cos(\beta). \quad (2.2)$$

North, N , East, E , and depth, D , are then calculated as:

$$N = R_h \cos(\psi) ; \quad (2.3)$$

$$E = R_h \sin(\psi) ; \quad (2.4)$$

$$D = R_s \sin(\beta). \quad (2.5)$$

2.3.2 USBL System Orientation

The USBL transceiver has several transponders very close together (hence ultra-short baseline), which contribute to measurement uncertainty due to shadowing of the transponders at shallow depression angles ($\beta < 45^\circ$). This results in optimal tracking falling in a cone-shaped area directly below the USBL transceiver when it is mounted vertically. This is problematic for UI AUV applications because typical tracking situations require AUV depths of 0-40 meters and a lateral offset (east direction presented hereafter) of up to 50 meters between the AUV and the surface ship. Therefore, the USBL investigations included the effect of transceiver tilt (see Figure 2.3) on the uncertainty of tracking the position of the AUV along the prescribed trajectory.

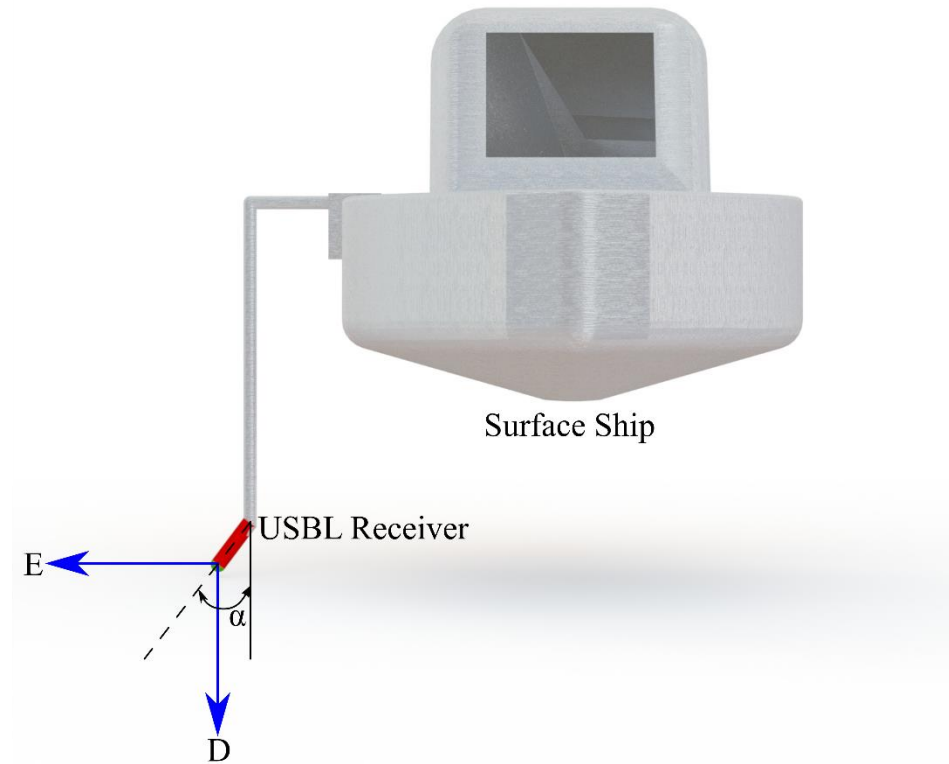


Figure 2.3: Tilt angle, α , of the USBL transceiver about the North axis of the transceiver reference frame. The origin of the transceiver reference frame is fixed to the end of the USBL transceiver; E is the East direction and D is depth.

In a typical configuration, the USBL transceiver is mounted approximately one meter below the bottom of the surface ship using an attachment rig (see Figure 2.3). The tilt angle, α , rotates the USBL transceiver about the North axis of the origin of the transceiver coordinate frame. In this example a positive tilt angle points the USBL transceiver away from the surface ship in the East, E , direction.

2.3.3 USBL in Global Reference Frame

It is important to note that the USBL system measures AUV position relative to the location of the transceiver. The objective of field testing is to determine the position of the AUV within the measurement range, which is in the global reference frame. Bringing the USBL measurement into the global reference frame introduces further uncertainty to the system based on the transceiver position and orientation in the water, described by GPS location, pitch, roll, yaw, and heave. The pitch, ϕ , and roll, θ , of the ship will affect the

USBL system's measurement of the depression angle, β . If the measurement of the ship pitch and roll are perfectly known, the depression angle can be corrected to account for the rotations, but if there is any error in these measurements, further uncertainty is introduced to the depression angle measurement. The ship's orientation, along with its GPS location, is necessary in transforming the USBL position measurement into the global reference frame.

2.4 Monte Carlo Simulation

Monte Carlo methods are a tool that can be used to solve probabilistic or deterministic problems. Probabilistic Monte Carlo methods utilize random numbers to simulate the physical random processes of a system [24]. This allows the propagation of uncertainty distributions, Gaussian or non-Gaussian, through a system of equations to simulate these physical processes. The USBL uncertainty is being evaluated using Monte Carlo Methods rather than directly inputting the USBL measurements to the measurement model of the AUV extended Kalman filter. This is due to interdependency of the USBL measurements (slant range, depression angle, and heading angle) and the position estimates.

Monte Carlo simulations were conducted for two cases: USBL measurement uncertainty in the USBL transceiver reference frame, and USBL measurement uncertainty in the global reference frame. The first case involves only the uncertainty in the USBL system based on the acoustic communication between the USBL transceiver and the AUV receiver. This allows for an understanding of the uncertainties involved in the measurements taken by the USBL system alone. The second case adds additional uncertainty because it requires knowledge of the USBL transceiver location and orientation to transform the measurement into the global reference frame. Performing these two analyses is beneficial because individual sources of uncertainty can be investigated, (e.g. the effect of the USBL transceiver pitch or GPS location), and then a case can be made for which measurements must have high precision and which are of lesser influence on the USBL position measurement of the AUV.

2.4.1 USBL Configurations for Monte Carlo Simulations

Monte Carlo simulations were conducted for three USBL configurations: transceiver oriented vertically (tilt angle $\alpha = 0$), transceiver tilted to $\alpha = 15^\circ$, and transceiver tilted to

$\alpha = 30^\circ$. A long baseline (LBL) array configuration (four transponders, $100m$ square grid) was also simulated as a baseline standard for direct comparison. For each Monte Carlo simulation, a fixed-depth analysis (at $D=10m$) was performed to investigate the measurement uncertainty in the $N-E$ plane (horizontal plane shown at bottom of Figure 2.4) and a fixed-North analysis was performed to investigate the position uncertainty in the $E-D$ plane (vertical plane, Figure 2.4 top).

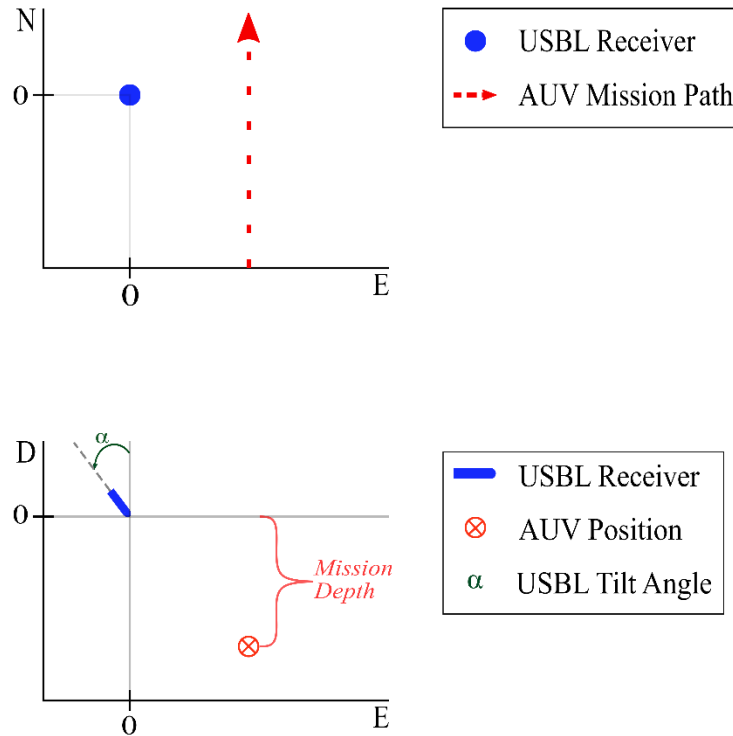


Figure 2.4: Fixed-depth (top) and fixed-north (bottom) analysis planes during USBL Monte Carlo simulations. The fixed-depth plane shows the $N-E$ plane (horizontal slice of water) at the depth ($10m$) of the AUV target, and the fixed-north analysis plane shows the $D-E$ plane (vertical slice) at a prescribed north distance from the USBL transceiver.

2.4.2 Ship Referenced Monte Carlo Simulation and Modeled Uncertainty

The Monte Carlo simulations were performed over a specified range of $N-E-D$ positions. During simulation, the slant range, R_s , depression angle, β , heading angle, ψ , and acoustic time, t_{R_s} , were calculated for each $N-E-D$ position without uncertainty according to:

$$R_s = \sqrt{N^2 + E^2 + D^2} ; \quad (2.6)$$

$$\beta = \text{atan2}(-D, \sqrt{E^2 + D^2}) ; \quad (2.7)$$

$$\gamma = \text{atan2}(E, N) ; \quad (2.8)$$

$$t_{R_s} = \frac{R_s}{c}, c = 1500 \text{ m/s}, \quad (2.9)$$

where c is the speed of sound [24] in water and atan2 is the quadrant-specific arctangent function. Initial measurement uncertainty was introduced in the simulations by creating noisy measurements of the speed of sound in water, c , and the acoustic time, t_{R_s} . To create a noisy measurement (denoted by the hat ^ symbol), Gaussian noise uncertainties ω_c and ω_t were added to the speed of sound and acoustic time, respectively, according to:

$$\hat{c} = c + W_c ; \quad (2.10)$$

$$\hat{t}_{R_s} = t_{R_s} + W_t. \quad (2.11)$$

The standard deviations used to generate the Gaussian noise terms were based on typical manufacturer's specifications. The Gaussian distributions are denoted by:

$$X \sim (m_x, S^2), \quad (2.12)$$

where X is a random variable with a true mean of μ_x and a variance of σ^2 . Here, it was assumed that the speed of sound uncertainty is $\omega_c \sim (0, \sigma_c^2)$ where $\sigma_c = 0.25 \text{ m/s}$ [25] and the acoustic time uncertainty is $\omega_t \sim (0, \sigma_t^2)$ where $\sigma_t = 125 \mu\text{sec}$ [26]. These noise terms propagated directly through the calculation of the slant range as:

$$\hat{R}_s = \hat{t}_{R_s} \hat{c}. \quad (2.13)$$

Both depression angle and heading angle have noise magnitudes (standard deviations of Gaussian models) that are dependent on the measured depression angle, β , due to transducer geometry and shadowing effects. The correlations (based on manufacturer's specifications) shown in Figure 2.5 were used to determine the noise magnitudes for both depression angle and heading angle, which are used to generate the noisy measurements:

$$\hat{b} = b + w_b ; \quad (2.14)$$

$$\hat{y} = y + w_y, \quad (2.15)$$

where $\omega_\beta = f(\beta)$ and $\omega_\psi = g(\beta)$ are the measurement noise for the depression and heading angles respectively. Functions $f(\beta)$ and $g(\beta)$ are shown in Figure 2.5.

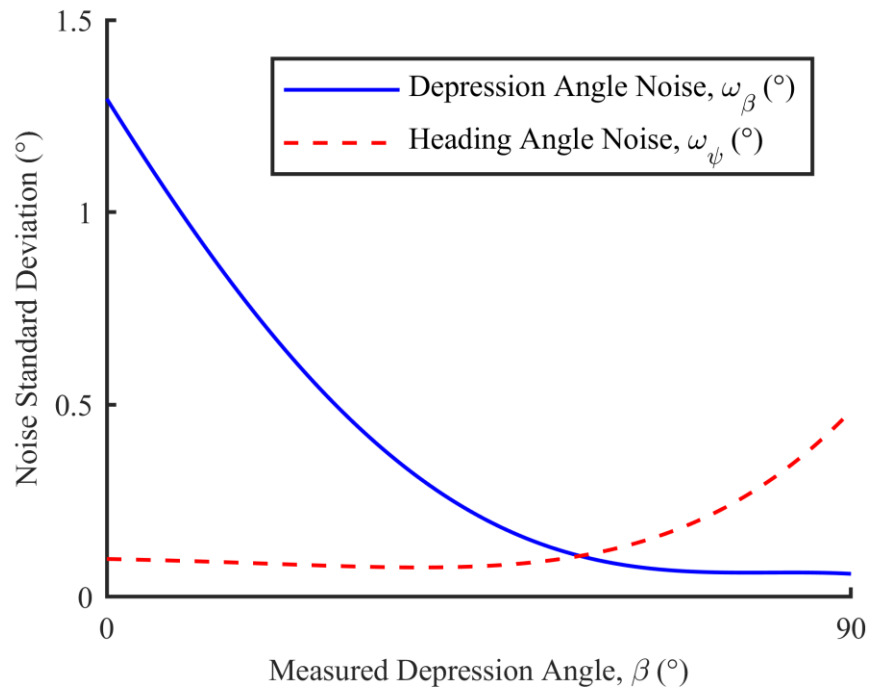


Figure 2.5: Measurement noise model for depression and heading angles. The magnitude (standard deviation of a Gaussian distribution) of heading angle noise, ω_β , increases rapidly for shallow depression angles ($\beta < 45^\circ$) due to shadowing effects.

The noise in the slant range, depression angle, and heading angle propagates through to the positional measurements as:

$$\hat{R}_h = \hat{R}_s \cos(\hat{\beta}); \quad (2.16)$$

$$\hat{N} = \hat{R}_h \cos(\hat{\psi}); \quad (2.17)$$

$$\hat{E} = \hat{R}_h \sin(\hat{\psi}); \quad (2.18)$$

$$\hat{Z} = \hat{R}_s \sin(\hat{\beta}); \quad (2.19)$$

The previous calculations (equations 2.6-2.19) create noisy measurements of the location of the transponder on the AUV. In the Monte Carlo simulations, these measurements are repeated with randomized Gaussian noise for each N - E - D position n times which allows for the determination of the total position measurement uncertainty:

$$u_{\hat{N}} = \sqrt{\frac{1}{n} \sum (\hat{N} - N)^2}; \quad (2.20)$$

$$u_{\hat{E}} = \sqrt{\frac{1}{n} \sum (\hat{E} - E)^2}; \quad (2.21)$$

$$u_{\hat{D}} = \sqrt{\frac{1}{n} \sum (\hat{D} - D)^2}; \quad (2.22)$$

$$u_{\hat{T}} = \sqrt{u_{\hat{N}}^2 + u_{\hat{E}}^2 + u_{\hat{D}}^2}, \quad (2.23)$$

where $u_{\hat{N}}, u_{\hat{E}}, u_{\hat{D}}$, are the uncertainties in the North, East, and depth measurements, respectively. The total positional uncertainty, $u_{\hat{T}}$, combines the uncertainty in each Cartesian direction.

2.4.3 Geo-Referenced USBL Uncertainty Monte Carlo

When transforming the AUV position measured by the USBL system into the global reference frame, additional uncertainty is added into the system. The uncertainty in the USBL transceiver position and orientation can greatly affect the measurement of the AUV position. It is assumed that the noise in the roll and pitch measurements directly affect the measurement uncertainty of the depression angle, b , therefore the ship pitch and roll uncertainty will be added to the noisy depression angle measurement using the root-sum-

squared method. The uncertainty in the ship's heading, ψ_{ship} , is assumed to be independent of the USBL's depression angle measurement and can therefore simply be added directly into the noisy measurement of the heading angle measurement of the USBL system. Uncertainty in the GPS location of the surface ship results in a known area for the position of the ship. Typical GPS documentation reports uncertainties separately as horizontal uncertainty and vertical uncertainty, which suggests the horizontal uncertainty would relate to the longitude and latitude measurements, but not the altitude measurements. Additionally, the reported uncertainty in GPS units is typically stated as $\pm\sigma_{GPS}$ which further suggests that it is a radial uncertainty that equally effects the latitude and longitude measurement. Therefore, the GPS horizontal uncertainty can be modeled as a radial uncertainty that can be directly added to the horizontal range measurement.

An additional Monte Carlo simulation study was performed that included these transceiver position and orientation uncertainties for a typical vertical mounting of the USBL transceiver. The additional uncertainty sources are applied to the USBL measurements, modifying equations 2.13-2.15 to produce:

$$\hat{\beta} = \beta + \omega_{\beta} + \sqrt{\omega_{\phi}^2 + \omega_{\theta}^2} ; \quad (2.24)$$

$$\hat{\psi} = \psi + \omega_{\psi} + \omega_{\psi,Ship} ; \quad (2.25)$$

$$\hat{R}_h = \hat{R}_s \cos(\hat{\beta}) + \omega_{GPS} ; \quad (2.26)$$

where ω_{ϕ} is the uncertainty in the USBL transceiver pitch orientation measurement; ω_{θ} is the uncertainty in the USBL transceiver roll orientation measurement; ω_{ψ} is the uncertainty in the USBL transceiver yaw or heading orientation measurement; and ω_{GPS} is the uncertainty in the USBL transceiver GPS position. The uncertainty in the USBL transceiver pitch, roll, and yaw measurements are introduced through a motion reference unit (MRU) mounted on the ship and position uncertainty is introduced through the ship mounted GPS unit.

The error in the pitch and roll measurements of the USBL transceiver orientation is assumed to directly affect the measurement of the depression angle in addition to the noise present in the depression angle measurement. Therefore, the root-sum-squared method is

used to include these Gaussian distributions in the noisy depression angle measurement, $\hat{\beta}$. The error in the transceiver heading measurement is assumed to directly impact the noisy heading measurement, $\hat{\psi}$. GPS accuracy is typically reported in terms of vertical accuracy, which refers to the altitude or elevation accuracy, and horizontal accuracy, which refers to the accuracy in determining the latitude and longitude of the target. Therefore, it is assumed that the horizontal accuracy is a radial factor and can be directly added to the noisy horizontal range, \hat{R}_h , which would then propagate the GPS uncertainty to the noisy North and East position estimates.

This study allows for determining the greatest sources of uncertainty in the AUV position. This information can then be used to inform future equipment requisitions to improve system performance in the most cost-effective manner.

2.5 Extended Kalman Filter

The extended Kalman filter (EKF) is a state estimator for nonlinear systems, adapted from the linear Kalman filter [27]. The EKF applied to a nonlinear system is denoted as:

$$x_k = f_{k-1}(x_{k-1}, u_{k-1}, w_{k-1}), \quad (2.27)$$

with the measurement model:

$$y_k = h_k(x_k, v_k), \quad (2.28)$$

where the subscript k denotes the time step; x is the state vector; f is the nonlinear propagation model; h is the nonlinear measurement model; u is the system inputs; w and v are white noise, i.e., zero-mean Gaussian noise, with known covariance matrices Q and R , such that:

$$w_k \sim (0, Q_k); \quad (2.29)$$

$$v_k \sim (0, R_k). \quad (2.30)$$

The system model used within the EKF must be observable for the EKF to converge and be able to estimate all system states. The filter is initialized with:

$$\hat{x}_0^+ = E(x_0) ; \quad (2.31)$$

$$P_0^+ = E \left[(x_0 - x_0^+) (x_0 - x_0^+)^T \right], \quad (2.32)$$

where E denotes the expected values; \hat{x}^+ is the *a posteriori* state estimate and P^+ is the state estimate covariance matrix. Next, the filter is propagated to the next time step. The system is linearized about estimates of the state and noise by:

$$F_{k-1} = \left. \frac{\partial f_{k-1}}{\partial x} \right|_{\hat{x}_{k-1}^+}, \quad (2.33)$$

$$L_{k-1} = \left. \frac{\partial f_{k-1}}{\partial w} \right|_{\hat{x}_{k-1}^+}, \quad (2.34)$$

and the time update obtains the *a priori* state and covariance estimates:

$$\hat{x}_k^- = f_{k-1}(\hat{x}_{k-1}^+, u_{k-1}, \mathbf{0}) ; \quad (2.35)$$

$$P_k^- = F_{k-1} P_{k-1}^+ F_{k-1}^T + L_{k-1} Q_{k-1} L_{k-1}^T. \quad (2.36)$$

Next, the measurement model is linearized about this *a priori* state estimate such that:

$$H_k = \left. \frac{\nabla h_k}{\nabla x} \right|_{\hat{x}_k^-}; \quad (2.37)$$

$$M_k = \left. \frac{\partial h_k}{\partial v} \right|_{\hat{x}_k^-}. \quad (2.38)$$

Finally, this state estimate is corrected using the measurements, creating the *a posteriori* estimate via:

$$K_k = P_k^- H_k^T (H_k P_k^- H_k^T + M_k R_k M_k^T)^{-1}; \quad (2.39)$$

$$\hat{x}_k^+ = \hat{x}_k^- + K_k [y_k - h_k(\hat{x}_k^-, \mathbf{0})]; \quad (2.40)$$

$$P_k^+ = (I - K_k H_k) P_k^- (I - K_k H_k)^T + K_k R_k K_k^T \quad (2.41)$$

where K is the so called Kalman gain used to scale the correction term based on the state, measurement and process noise covariance matrices; $y_k - h_k(\hat{x}_k^-, \mathbf{0})$ is the correction term

which compares the measurement against the measurement model at time k to update the state estimate. This process is performed as the AUV operates to provide real-time state estimates.

2.6 Depth Estimation EKF

Five different EKF cases were programmed and evaluated using MATLAB[®] and data from UI AUV field test missions. The first EKF case, presented in section 2.6.1, is a baseline EKF for comparing against the following cases and it confirms that the post-process EKF produces similar results to the onboard EKF. The second EKF case, described in section 2.6.2, investigates the influence of adding USBL North and East position measurements to the EKF. EKF case three, section 2.6.3, provides a baseline filter with AUV depth as a state for comparison with USBL performance as well as verifying the observability of the system with the added depth state. EKF case four, described in section 2.6.4, investigates the response of the EKF case to including USBL North, East, and depth position measurements. Finally, EKF case 5, presented in section 2.6.5, provides a best-case USBL scenario. This EKF combines the AUV depth with the USBL North and East position as well as USBL depth from telemetry. Since the depth measurement of USBL systems have significantly greater uncertainty than the North and East measurement uncertainty, some manufacturers include a pressure transducer depth sensor within the USBL and communicates the depth using a delayed communication ping from the AUV mounted USBL. This telemetry depth greatly reduces the measurement uncertainty of the USBL system.

2.6.1 Legacy EKF and Case 1: Post-Process EKF

The legacy EKF case includes the system states: local east position, E ; local north position, N ; relative speed, s ; AUV heading, ψ , east current, c_E ; and north current, c_N . additionally, it includes a gyroscope measurement, $\dot{\psi}$, as a driving function. The propagation model for this EKF is:

$$x_k = f_{k-1}(x_{k-1}, u_{k-1}, w_{k-1}) = \begin{bmatrix} E + s \sin(\psi) \Delta t + c_E \Delta t + w_E \\ N + s \cos(\psi) \Delta t + c_N \Delta t + w_N \\ s + w_s \\ \psi + \dot{\psi} \Delta t + w_\psi \\ c_E + w_{c_E} \\ c_N + w_{c_N} \end{bmatrix}_{k-1};$$

$$x = \begin{bmatrix} E & N & s & \psi & c_E & c_N \end{bmatrix}^T;$$

$$u = \dot{\psi};$$

$$w = \begin{bmatrix} w_E & w_N & w_s & w_\psi & w_{c_E} & w_{c_N} \end{bmatrix}^T, \quad (2.42)$$

where x is the state vector, f is the system propagation model, u is the driving function, w is the vector of the noise associated with each state (e.g. w_E is the noise associated with the propagation of the local East position), and Δt is the discrete time step.

This EKF is updated with four LBL range measurements, r_A - r_D , an AUV speed measurement, s_m , and an AUV heading measurement, ψ_m . These measurements are introduced to the EKF through the following measurement model:

$$y_k = h_k(x_k, v_k) = \begin{bmatrix} \sqrt{(E - A_E)^2 + (N - A_N)^2 + (Z - A_Z)^2} + v_A \\ \sqrt{(E - B_E)^2 + (N - B_N)^2 + (Z - B_Z)^2} + v_B \\ \sqrt{(E - C_E)^2 + (N - C_N)^2 + (Z - C_Z)^2} + v_C \\ \sqrt{(E - D_E)^2 + (N - D_N)^2 + (Z - D_Z)^2} + v_D \\ s + v_{s_m} \\ \psi + v_{\psi_m} \end{bmatrix}_k ;$$

$$y = [r_A \quad r_B \quad r_C \quad r_D \quad s_m \quad \psi_m]^T ;$$

$$v = [v_A \quad v_B \quad v_C \quad v_D \quad v_{s_m} \quad v_{\psi_m}]^T ; \quad (2.43)$$

where y is the measurement vector; h is the system measurement model; v is the vector of the noise associated with each measurement (e.g. v_A is the noise associated with the measurement of the acoustic range from buoy A); A_E , A_N , and A_Z are the East, North, and depth position of buoy A in the transceiver reference frame (likewise for B - D); Z is the AUV depth directly from the onboard pressure sensor.

During field testing, the UI AUVs record the onboard EKF state estimates in addition to all onboard measurements. This allows for post-processing field tests and verifying onboard EKF estimates of the AUV path. A post-process EKF that contains the same states and measurements as the onboard EKF provides a baseline for comparison as states and measurements are added to the EKF. The legacy EKF onboard the UI AUV is an observable system, which means that the EKF will converge and can estimate all system states. The post-process EKF utilizes the same states, measurements, propagation model, and measurement model as the legacy EKF; therefore, the post-process EKF is also observable. This post-process EKF will be referred to as *Case 1: Post-Process EKF* hereafter.

2.6.2 Case 2: Post-Process EKF plus USBL North and East Measurements

This EKF case leaves the system model, i.e., $x_k = f_{k-1}(x_{k-1}, u_{k-1}, w_{k-1})$, unchanged but modifies the measurement by adding North and East position measurements from the USBL system. The USBL measurements are added as the seventh and eighth rows of the measurement model as follows:

$$\begin{bmatrix} E_{USBL} \\ N_{USBL} \end{bmatrix}_{k+1} = \begin{bmatrix} E + v_{E_{USBL}} \\ N + v_{N_{USBL}} \end{bmatrix}_k ; \quad (2.44)$$

where $v_{E_{USBL}}$ is the USBL East position measurement uncertainty and $v_{N_{USBL}}$ is the USBL North position measurement uncertainty. These USBL uncertainties will be calculated via Monte Carlo Simulation as described in sections 2.3.3. This changes the measurement vector, y , to:

$$y = [r_A \quad r_B \quad r_C \quad r_D \quad s_m \quad \psi_m \quad E_{USBL} \quad N_{USBL}]^T, \quad (2.45)$$

Adding these measurements to the system maintained the observability of the system; therefore, the EKF will still be valid.

2.6.3 Case 3: Post-Process EKF plus AUV Depth

This EKF case adds the AUV depth as a state in the propagation model as well as adding the depth to the measurement model as an individual measurement. The depth inserted to the third row of the system model by:

$$[Z]_{k+1} = [Z + w_Z]_k, \quad (2.46)$$

where w_Z is the process noise of the depth state, estimated from previous AUV field tests.

The addition of the depth state results in the new state vector:

$$x = [E \quad N \quad Z \quad s \quad \psi \quad c_E \quad c_N]^T, \quad (2.47)$$

The measurement model adds depth to the seventh row by:

$$[Z_m]_k = [Z + v_Z]_k, \quad (2.48)$$

where v_Z is the measurement noise of the AUV pressure transducer depth sensor; Z_m is the measured depth of the AUV plus measurement noise. The mission depth is assumed to be

constant; therefore, depth is directly measured by the depth sensor plus Gaussian noise. The new measurement vector, y , is then:

$$y = [r_A \quad r_B \quad r_C \quad r_D \quad s_m \quad \psi_m \quad Z_m]^T, \quad (2.49)$$

The addition of the depth measurement and state maintained the observability of the system; therefore, the EKF will be able to estimate all the states in the system.

2.6.4 Case 4: Post-Process EKF plus USBL North, East, and Depth Measurements

Case 4 adds depth as a state and the North, East, and depth measurements from the USBL to the onboard EKF case. The system model, $x_k = f_{k-1}(x_{k-1}, u_{k-1}, w_{k-1})$, is identical to case 3, where the depth state was added to the current EKF model. The USBL measurements are added to the system as the seventh, eighth, and ninth rows as follows:

$$\begin{bmatrix} E_{USBL} \\ N_{USBL} \\ Z_{USBL} \end{bmatrix}_{k+1} = \begin{bmatrix} E + v_{E_{USBL}} \\ N + v_{N_{USBL}} \\ Z + v_{Z_{USBL}} \end{bmatrix}_k; \quad (2.50)$$

where $v_{E_{USBL}}$ and $v_{N_{USBL}}$ are the same as in case 2 above and $v_{Z_{USBL}}$ is the USBL depth measurement uncertainty. Due to the addition of these measurements, the measurement vector is now:

$$y = [r_A \quad r_B \quad r_C \quad r_D \quad s_m \quad \psi_m \quad E_{USBL} \quad N_{USBL} \quad Z_{USBL}]^T, \quad (2.51)$$

The addition of these three measurements and the depth state did not affect the system observability; therefore the EKF will be able to estimate the system states.

2.6.5 Case 5: Post-Process EKF plus AUV Depth, USBL North and East Measurements, and USBL Telemetry Depth Measurements

The final case is the combination of cases two and three as well as utilizing the USBL depth from telemetry. The resultant system model is the same as cases three and four above, i.e. the legacy EKF scheme plus a depth state. The measurement model is the combination of cases three and four plus the USBL telemetry depth. Therefore, the measurements are:

$$y = [r_A \ r_B \ r_C \ r_D \ s_m \ \psi_m \ Z_m \ E_{USBL} \ N_{USBL} \ Z_{Telem}]^T, \quad (2.52)$$

where Z_m , is the depth measurement from the AUV pressure transducer and Z_{Telem} is the depth measurement from the AUV-mounted USBL receiver, transmitted by a delayed telemetry ping. The AUV depth from telemetry is proportional to the time delay and is calculated by:

$$Z_{Telem} = \frac{10}{9} \Delta t - \frac{1000}{9}, \quad (2.53)$$

where Δt is the time delay between the response ping and the telemetry ping. This is implemented into the Monte Carlo using the following:

$$\begin{aligned} \hat{\Delta t} &= \frac{9}{10} \left(Z_{USBL_{press}} + \omega_{Z,USBL} \right) + 100 + \omega_{\Delta t}; \\ \hat{Z}_{Telem} &= \frac{10}{9} \hat{\Delta t} - \frac{1000}{9}, \end{aligned} \quad (2.54)$$

where the carat symbol (^) represents noisy measurement; $Z_{USBL_{press}}$ is the depth measurement from the USBL pressure transducer; $\omega_{Z,USBL}$ is the uncertainty in the pressure depth measurement; $\omega_{\Delta t}$ is the uncertainty in the delay time due to transmission time and clock time uncertainties. This telemetry communication is an effective method of communication because the AUV velocity, approximately 0.85 m/s , is significantly smaller than the speed of sound through water, approximately 1500 m/s , meaning the difference in AUV position is negligible. This modified system is still fully observable; therefore, the EKF can estimate all system states.

2.7 EKF Covariance Matrices

The covariance matrices describe the noise characteristics of the propagation model, measurement model, and the estimate of the state. Equations 2.40, 2.43, and 2.45 show how the various covariance matrices interact together; both Q and R are involved in the calculation of the Kalman gain, K , and the *a posteriori* state covariance matrix, P_k^+ . Generally, large values in Q indicate large uncertainty in the propagation model and large values in R indicate large uncertainties in the measurements and measurement model. Ideally, all noise values in the covariance matrices would be Gaussian and could be readily determined to a high precision. Generally, this is not feasible, whether through linear approximations, unknown dynamics, or other sources; therefore, an estimate for these values can be used as a starting point and then the values can be adjusted to influence the filter behavior. Typically, the process, Q , and measurement, R , noise covariance matrices are assumed to be constant in time. The *Case 1: Post-Process EKF* and the *Case 3: Post-Process EKF plus AUV Depth* follow this convention. EKF *Case 2, 4, and 5* hold all noise covariances constant except for the USBL measurement noise covariance values in R because the USBL measurement uncertainty changes due to the AUV position relative to the USBL transceiver location.

2.7.1 Process Noise Covariance Matrix

The process noise covariances describe the inaccuracies present in the EKF propagation model. The process noise inaccuracies come from sources such as linear approximations and unknown system dynamics. Given that the inaccuracies are not due to a measurement device, they are difficult to precisely quantify and therefore are estimated. The estimations are derived from typical error bounds associated with the propagation of the state observed in field tests. The noise associated with each state is assumed to be uncorrelated, i.e. the process noise of the East state, w_E , is not affected by the process noise of the North state, w_N , or any other states. Therefore, the process noise covariance can be represented as a diagonal matrix. As depth has not historically been an included state within the UI AUVs, an estimate of process noise was determined through analysis of historical AUV field tests. This value of 0.10859 m indicates that the process noise for the depth state propagation is similar

to that of the East and North state process noise. Table 2.1 indicates which process noise terms are included in each EKF case presented in this paper as well as the respective values for each. The form of the process noise covariance matrix is therefore:

$$Q = \text{diag}\left(\left[\sigma_1^2, \sigma_2^2, \dots, \sigma_n^2 \right]\right), \quad (2.55)$$

where S_i is the process noise of state x_i and S_n is the process noise of the n^{th} state. Table 2.1 shows that *Case 1* and *Case 2* do not include a process noise value for depth because these EKF cases do not include a depth state, while the other cases add depth as a state and use various measurements.

Case 1 and *Case 2* both have the same states and therefore have the same process noise covariance matrix, Q , in the form:

$$Q = \text{diag}\left(\left[\sigma_{w_E}^2 \quad \sigma_{w_N}^2 \quad \sigma_{w_s}^2 \quad \sigma_{w_\psi}^2 \quad \sigma_{w_{cE}}^2 \quad \sigma_{w_{cN}}^2 \right]\right); \quad (2.56)$$

where σ_{w_E} is the process noise of the East state; σ_{w_N} is the process noise of the North state; σ_{w_s} is the process noise of the speed state; σ_{w_ψ} is the process noise of the heading state; $\sigma_{w_{cE}}$ is the process noise of the east current state; $\sigma_{w_{cN}}$ is the process noise of the north current state. This noise is propagated through the EKF by equation 2.10, applying the process noise to the determination of the *a priori* state covariance.

Case 3, 4, and 5 add depth as a state. The resulting process noise covariance matrix, Q , for these cases are in the form:

$$Q = \text{diag}\left(\left[\sigma_{w_E}^2 \quad \sigma_{w_N}^2 \quad \sigma_{w_z}^2 \quad \sigma_{w_s}^2 \quad \sigma_{w_\psi}^2 \quad \sigma_{w_{cE}}^2 \quad \sigma_{w_{cN}}^2 \right]\right); \quad (2.57)$$

where σ_{w_z} is the process noise of the depth state.

TABLE 2.1: PROCESS NOISE VARIANCE VALUES

| Case | 1 | 2 | 3 | 4 | 5 |
|-------------------------|--------------|---------------------------|--------------------------|-----------------------------|---|
| EKF Case Description | Post-Process | Post-Process + USBL (N,E) | Post-Process + AUV Depth | Post-Process + USBL (N,E,Z) | Post-Process + AUV Depth + USBL (N,E) + Telemetry Depth |
| σ_{w_E} [m] | 0.1 | 0.1 | 0.1 | 0.1 | 0.1 |
| σ_{w_N} [m] | 0.1 | 0.1 | 0.1 | 0.1 | 0.1 |
| σ_{w_Z} [m] | - | - | 0.10859 | 0.10859 | 0.10859 |
| σ_{w_s} [m/s] | 0.1 | 0.1 | 0.1 | 0.1 | 0.1 |
| σ_{w_ψ} [deg] | 5.0 | 5.0 | 5.0 | 5.0 | 5.0 |
| $\sigma_{w_{cE}}$ [m/s] | 0.001 | 0.001 | 0.001 | 0.001 | 0.001 |
| $\sigma_{w_{cN}}$ [m/s] | 0.001 | 0.001 | 0.001 | 0.001 | 0.001 |

2.7.2 Measurement Noise Covariance Matrix

The measurement noise covariance matrix describes the noise associated with each measurement used within the EKF. The measurement noise is assumed to be uncorrelated, similar to the process noise covariance, and therefore is diagonal in form, i.e.:

$$R = \text{diag}\left(\left[\sigma_1^2, \sigma_2^2, \dots, \sigma_n^2 \right]\right); \quad (2.58)$$

where the subscript denotes the measurement number and σ_n is the uncertainty of the nth measurement. The covariance values used for each measurement are either estimated through post-process analysis of previous field testing data or using manufacturer's published uncertainties. For more information on the measurement noise values for the onboard EKF, see [15].

The legacy EKF, as well as the *Case 1* EKF, has a measurement noise covariance matrix in the form:

$$R = \text{diag}\left(\left[\sigma_{v_A}^2 \quad \sigma_{v_B}^2 \quad \sigma_{v_C}^2 \quad \sigma_{v_D}^2 \quad \sigma_{v_{s_m}}^2 \quad \sigma_{v_{\psi_m}}^2 \right]\right); \quad (2.59)$$

where $\sigma_{v_A} - \sigma_{v_D}$ are the measurement noise for each LBL range; $\sigma_{v_{s_m}}$ is the speed measurement noise; $\sigma_{v_{\psi_m}}$ is the heading measurement noise. These values, determined from historic UI AUV field testing, are held constant with all EKF cases presented in this paper.

The *Case 2* EKF adds East and North position measurements from the USBL to the EKF, resulting in a measurement covariance matrix in the form:

$$R = \text{diag} \left(\left[\sigma_{v_A}^2 \quad \sigma_{v_B}^2 \quad \sigma_{v_C}^2 \quad \sigma_{v_D}^2 \quad \sigma_{v_{s_m}}^2 \quad \sigma_{v_{\psi_m}}^2 \quad \sigma_{v_{EUSBL}}^2 \quad \sigma_{v_{NUSBL}}^2 \right]_k \right); \quad (2.60)$$

where $\sigma_{v_{EUSBL}}$ and $\sigma_{v_{NUSBL}}$ are the measurement noise of the USBL East and North measurements respectively; the subscript k is the time step. These measurement noise values are determined from the Monte Carlo analysis described in section 2.3 based on the location of the AUV relative to the USBL transceiver. The time step, k , is included in this iteration of the measurement noise covariance matrix, R , because the USBL measurement uncertainties are dependent on the AUV position through time. Therefore, at each time step, k , the measurement uncertainty for the USBL measurements, E_{USBL} and N_{USBL} , changes due to the updated position measurement.

The *Case 3* EKF modifies *Case 1* by adding a depth measurement from the AUV pressure sensor. The measurement noise covariance matrix is therefore populated by:

$$R = \text{diag} \left(\left[\sigma_{v_A}^2 \quad \sigma_{v_B}^2 \quad \sigma_{v_C}^2 \quad \sigma_{v_D}^2 \quad \sigma_{v_{s_m}}^2 \quad \sigma_{v_{\psi_m}}^2 \quad \sigma_{v_{z_m}}^2 \right] \right); \quad (2.61)$$

where $\sigma_{v_{z_m}}$ is the measurement noise of the AUV pressure transducer. This value was determined from the reported measurement uncertainty of the AUV onboard pressure sensor.

Case 4 adds the USBL depth measurement to *Case 2*, which gives the measurement noise covariance matrix as:

$$R = \text{diag} \left(\left[\sigma_{v_A}^2 \quad \sigma_{v_B}^2 \quad \sigma_{v_C}^2 \quad \sigma_{v_D}^2 \quad \sigma_{v_{s_m}}^2 \quad \sigma_{v_{\psi_m}}^2 \quad \sigma_{v_{EUSBL}}^2 \quad \sigma_{v_{NUSBL}}^2 \quad \sigma_{v_{zUSBL}}^2 \right]_k \right); \quad (2.62)$$

where $\sigma_{v_{zUSBL}}^2$ is the measurement noise of the USBL depth measurement. This noise value is determined by the Monte Carlo analysis in section 2.3. Again, it is important to note that this case includes the time step, k , due to the time varying uncertainty of the USBL system.

Case 5 combines *Cases 3* and *4*, i.e., it includes AUV depth measurement from the pressure transducer as well as the North and East measurements from the USBL. Additionally, this case exchanges the USBL calculated depth for a telemetry depth from the USBL receiver mounted on the AUV. The resulting measurement noise covariance matrix is:

$$R = \text{diag} \left(\left[\sigma_{v_A}^2 \quad \sigma_{v_B}^2 \quad \sigma_{v_C}^2 \quad \sigma_{v_D}^2 \quad \sigma_{v_{s_m}}^2 \quad \sigma_{v_{\psi_m}}^2 \quad \sigma_{v_{z_m}}^2 \quad \sigma_{v_{EUSBL}}^2 \quad \sigma_{v_{NUSBL}}^2 \quad \sigma_{v_{zTelem}}^2 \right]_k \right); \quad (2.63)$$

As with *Cases 3* and *4*, the measurement noise covariance matrix is time varying due to the USBL measurements.

Table 2.2 describes the noise terms present in each EKF case and the magnitudes of those values. The depth uncertainty has two values because the density difference between saltwater and freshwater directly affects the depth calculation from the pressure transducer. The USBL East measurement noise is found by:

$$\sigma_{v_{EUSBL}} = g_E(E, N, Z), \quad (2.64)$$

where $\sigma_{v_{EUSBL}}$ is the uncertainty in the East position measurement from the USBL; $g_E(E, N, Z)$ denotes the uncertainty in the East position is a function of the AUV North, East, and depth position. The Monte Carlo simulation performed in Section 2.4.3 determines this uncertainty value. The North and depth uncertainty values, $g_N(E, N, Z)$ and $g_Z(E, N, Z)$ respectively, are also determined by the Section 2.4.3 Monte Carlo simulation. The telemetry depth measurement noise is found by:

$$\sigma_{v_{Z,Telem}} = g_{Z,Telem}(E, N, Z) \quad (2.65)$$

where $\sigma_{v_{Z,Telem}}$ is the uncertainty in the USBL telemetry depth measurement; $g_{Z,Telem}(E, N, Z)$ denotes the uncertainty in the telemetry depth measurement is a function of the AUV North, East, and depth position. This uncertainty value is the standard deviation of the noisy telemetry depth measurement described in Equation 2.53, which is calculated by:

$$\sigma_{v_{Z,Telem}} = \sqrt{\frac{1}{n} \sum (\hat{Z}_{Telem} - Z_{Telem})^2}, \quad (2.66)$$

where the carat symbol (^) denotes the noisy measurement, n is the number of Monte Carlo iterations and Z_{Telem} is the depth from the USBL telemetry communication.

TABLE 2.2: MEASUREMENT NOISE COVARIANCE VALUES

| Case | 1 | 2 | 3 | 4 | 5 |
|------------------------------|--------------|---------------------------|---|-----------------------------|---|
| EKF Case Description | Post-Process | Post-Process + USBL (N,E) | Post-Process + AUV Depth | Post-Process + USBL (N,E,Z) | Post-Process + AUV Depth + USBL (N,E) + Telemetry Depth |
| σ_{v_A} [m] | 3.3 | 3.3 | 3.3 | 3.3 | 3.3 |
| σ_{v_B} [m] | 3.3 | 3.3 | 3.3 | 3.3 | 3.3 |
| σ_{v_C} [m] | 3.3 | 3.3 | 3.3 | 3.3 | 3.3 |
| σ_{v_D} [m] | 3.3 | 3.3 | 3.3 | 3.3 | 3.3 |
| $\sigma_{v_{sm}}$ [m/s] | 0.16 | 0.16 | 0.16 | 0.16 | 0.16 |
| $\sigma_{v_{\psi_m}}$ [deg] | 5.75 | 5.75 | 5.75 | 5.75 | 5.75 |
| $\sigma_{v_{Z_m}}$ [m] | - | - | $\begin{cases} 0.4977\text{m (saltwater)} \\ 0.5097\text{m (freshwater)} \end{cases}$ | - | $\begin{cases} 0.4977\text{m (saltwater)} \\ 0.5097\text{m (freshwater)} \end{cases}$ |
| $\sigma_{v_{E_{USBL}}}$ [m] | - | $g_E(E, N, Z)$ | - | $g_E(E, N, Z)$ | $g_E(E, N, Z)$ |
| $\sigma_{v_{N_{USBL}}}$ [m] | - | $g_N(E, N, Z)$ | - | $g_N(E, N, Z)$ | $g_N(E, N, Z)$ |
| $\sigma_{v_{Z_{USBL}}}$ [m] | - | - | - | $g_Z(E, N, Z)$ | - |
| $\sigma_{v_{Z_{Telem}}}$ [m] | - | - | - | - | $g_{Z,Telem}(E, N, Z)$ |

2.7.3 State Covariance Matrix

The state covariance matrix, P , is a measure of the state estimation covariance, i.e., the covariance associated with each estimated state. The diagonal entries of the state covariance matrix correspond to the uncorrelated state covariance while the other matrix entries give an estimate of the correlated state covariance. This matrix is updated as the EKF progresses through time and it denotes the covariance of the estimation error of the state estimation. This matrix is initialized as a diagonal matrix due to the assumption that the state covariance terms are uncorrelated. The initial values selected for P , affects the transient (initial) response of the EKF, where large values, denoting high uncertainty, cause the EKF to take longer to converge, while small values, denoting low uncertainty, result in the EKF converging more quickly. The initial planar position values, E and N , are determined by the AUV onboard GPS position. Thus, the state covariances are initialized by the estimated measurement uncertainty of the onboard GPS. The AUV depth measurement is reasonably accurate, but the reverse dive of the AUV coupled with mission beginning on the surface introduces perturbations to the system. The speed and heading measurements are also reasonably accurate but experience great perturbation during the reverse dive sequence.

Therefore, they are initialized with values greater than typical mission values to account for the unmodeled dynamics present in the AUV reverse dive. The water current state is initially assumed to be zero since there is no direct measurement of the water current. Given the lack of initial state information, the water current covariances are initialized with a large value compared to expected currents. Due to the large magnitude of the initial covariance estimates, the state covariance transient response will converge more slowly than if smaller values had been selected. This can be observed through the values within the P matrix as they converge and reach a relative steady state.

Table 2.3 describes the initial state covariance estimates used to initialize the EKF. It is worth noting that *Case 1* and *Case 2* do not include a depth state estimate because these EKF cases do not include a depth state.

Case 1 and *Case 2* have the same states and therefore have the same initial state covariance matrix:

$$P_0^+ = \text{diag} \left(\left[\begin{array}{cccccc} \sigma_{\hat{E}_0^+}^2 & \sigma_{\hat{N}_0^+}^2 & \sigma_{\hat{s}_0^+}^2 & \sigma_{\hat{\psi}_0^+}^2 & \sigma_{\hat{c}_{E,0}^+}^2 & \sigma_{\hat{c}_{N,0}^+}^2 \end{array} \right] \right); \quad (2.67)$$

where $\sigma_{\hat{E}_0^+}$ is the initial state covariance of the East position; $\sigma_{\hat{N}_0^+}$ is the initial state covariance of the North position; $\sigma_{\hat{s}_0^+}$ is the initial state covariance of the AUV speed; $\sigma_{\hat{\psi}_0^+}$ is the initial state covariance of the AUV heading; $\sigma_{\hat{c}_{E,0}^+}$ is the initial state covariance of the East current; $\sigma_{\hat{c}_{N,0}^+}$ is the initial state covariance of the North current.

Cases 3, 4, and 5 share the same states as *Case 1* and *Case 2* with the addition of the depth state. The addition of the depth state results in the initial state covariance matrix:

$$P_0^+ = \text{diag} \left(\left[\begin{array}{ccccccc} \sigma_{\hat{E}_0^+}^2 & \sigma_{\hat{N}_0^+}^2 & \sigma_{\hat{z}_0^+}^2 & \sigma_{\hat{s}_0^+}^2 & \sigma_{\hat{\psi}_0^+}^2 & \sigma_{\hat{c}_{E,0}^+}^2 & \sigma_{\hat{c}_{N,0}^+}^2 \end{array} \right] \right); \quad (2.68)$$

where $\sigma_{\hat{z}_0^+}$ is the initial state covariance of the AUV depth.

TABLE 2.3: INITIAL STATE COVARIANCE VALUES

| Case | 1 | 2 | 3 | 4 | 5 |
|----------------------------------|--------------|---------------------------|--------------------------|-----------------------------|---|
| EKF Case Description | Post-Process | Post-Process + USBL (N,E) | Post-Process + AUV Depth | Post-Process + USBL (N,E,Z) | Post-Process + AUV Depth + USBL (N,E) + Telemetry Depth |
| $\sigma_{\hat{E}_0^+}$ [m] | 5.0 | 5.0 | 5.0 | 5.0 | 5.0 |
| $\sigma_{\hat{N}_0^+}$ [m] | 5.0 | 5.0 | 5.0 | 5.0 | 5.0 |
| $\sigma_{\hat{Z}_0^+}$ [m] | - | - | 5.0 | 5.0 | 5.0 |
| $\sigma_{\hat{s}_0^+}$ [m/s] | 1.5 | 1.5 | 1.5 | 1.5 | 1.5 |
| $\sigma_{\hat{\psi}_0^+}$ [deg] | 20 | 20 | 20 | 20 | 20 |
| $\sigma_{\hat{c}_{E,0}^+}$ [m/s] | 1.0 | 1.0 | 1.0 | 1.0 | 1.0 |
| $\sigma_{\hat{c}_{N,0}^+}$ [m/s] | 1.0 | 1.0 | 1.0 | 1.0 | 1.0 |

Chapter 3: Results and Discussion

3.1. USBL Monte Carlo Simulation Results

3.1.1. Results in Transceiver Reference Frame

The transceiver reference frame Monte Carlo simulations were performed over a range of $\pm 40m$ in the North and East directions and depths of $0-40m$, centered at the USBL transceiver. A similar range was considered for an LBL simulation as a comparison against current UI AUV navigation methods. The LBL range was centered in the middle of four transponders located at the corners of a $100m$ square grid. At each $N-E-D$ position, an overall uncertainty was calculated from the position uncertainties for each individual axis.

Results from the LBL simulation are shown in Figure 3.1, which shows measurement uncertainty heatmaps for all three Cartesian directions (North, East, and depth) as well as the total uncertainty that combines all three. As can be seen, uncertainty is reasonably uniform in the three Cartesian directions, and is lowest at center of the range, where uncertainty is on the order of $0.25m$.

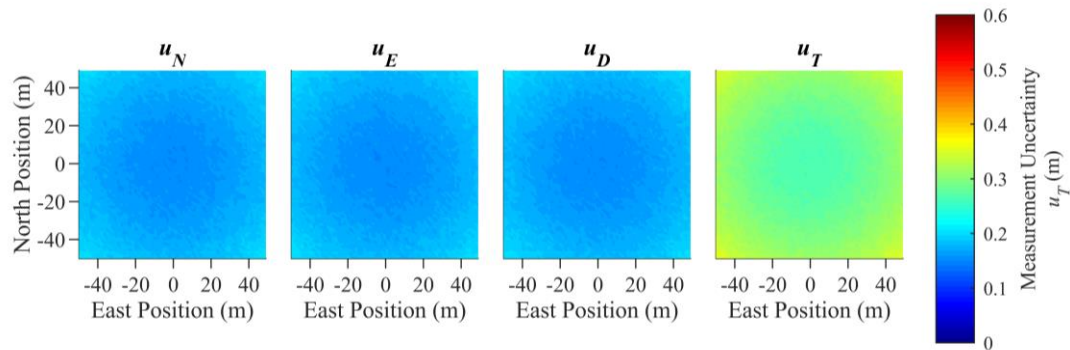


Figure 3.1: Measurement uncertainty heatmaps for LBL Monte Carlo simulation. All plots are $N-E$ slices at $D=10m$. The left three plots show uncertainties from North, East, and depth, from left to right. The right plot shows the total positional uncertainty.

The USBL localization system exhibits a much more localized region of accuracy compared to the LBL system. As indicated by multiple manufacturers, a cone-shaped region of minimal-uncertainty extends out from the direction of the USBL transponder. This is clearly seen in Figure 3.2, which shows heatmaps for a $N = 0m$ fixed-North plane for transceiver tilt angles of 0° , 15° , and 30° from left to right. In these heatmaps, the lowest uncertainty ($u_r \cong 0.2m$) is in the area extending out from the USBL transponder between $0m$ and $40m$ and depth angles greater than 45° . The white areas shown are regions outside the range of the uncertainty modeling. These results suggest that tilting the USBL transceiver head can advantageously shift the ideal measurement region, allowing the surface ship to be located at an East offset from the AUV path. Additionally, when mounted vertically, the results suggest that the minimum position uncertainty occurs when the AUV travels directly beneath the USBL transceiver.

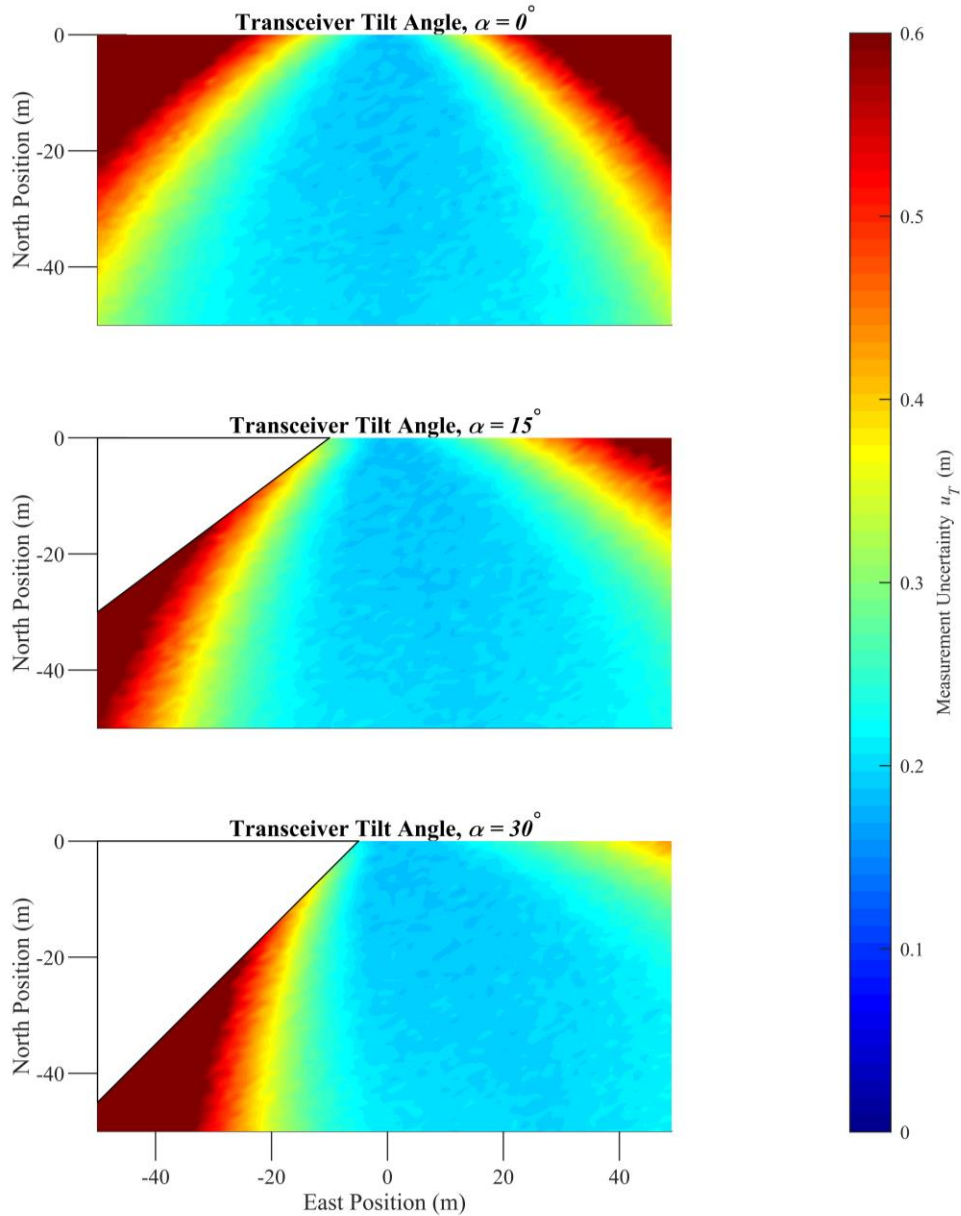


Figure 3.2: Measurement uncertainty heatmaps for $N=0$ fixed-north USBL configurations of zero tilt (Top), 15° tilt (Middle), 30° tilt (Bottom). The white areas are regions outside the range of the uncertainty modeling.

Figure 3.3 shows $N=0m$ fixed-North uncertainty Cartesian component heatmaps for the zero-tilt angle transceiver configuration. In these plots, depth is clearly the largest contributor to the positional uncertainty; this results from the increasing uncertainty in the measured depression angle at low depression angles (see Figure 2.5). It is interesting to note that the North uncertainty is significantly smaller than the depth uncertainty throughout the

measurement region and smaller than the East uncertainty at shallow depression angles ($\beta < 45^\circ$).

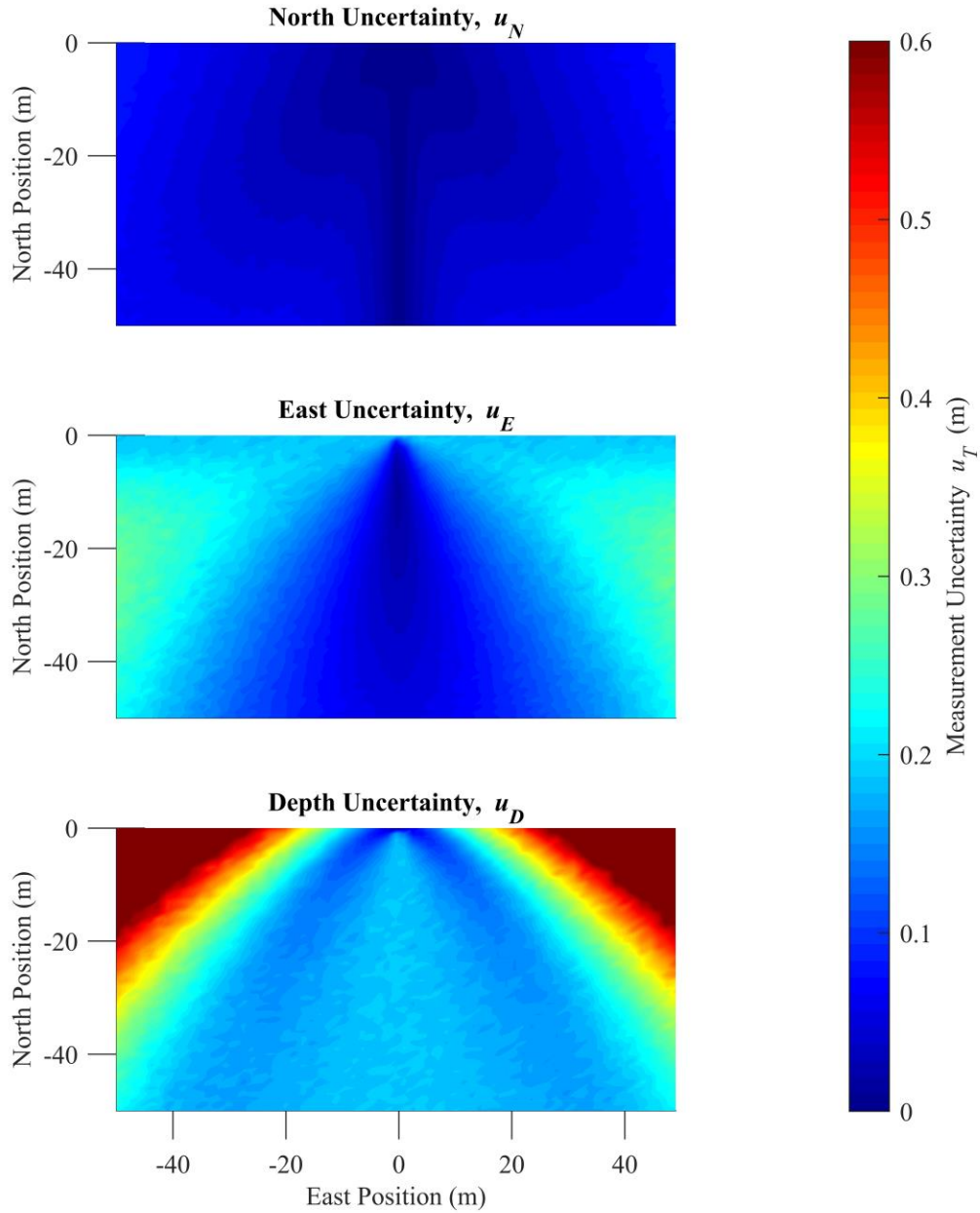


Figure 3.3: Measurement uncertainty heatmaps for $N=0$ fixed-north USBL configuration and of zero transceiver tilt. Top to bottom, heatmaps are shown for North, East, and depth. Total uncertainty is shown in the top plot in Figure 3.1.

Figure 3.4 shows results of fixed-depth Monte Carlo simulation performed at $D=10m$ for USBL transceiver tilt angles of 0° (bottom row), 15° (middle row), and 30° (top row). The uncertainties in the North (left column), East (center-left column), and depth (center-right column) directions in addition to total uncertainty (right column) are shown. The plots in Figure 3.3 reveal the cone shape from a top view, as well as highlighting some directional aspects of the USBL system. Specifically, the North and East uncertainties are significantly smaller than the depth uncertainty. This shows that at the selected depth, the primary contributor to the uncertainty of the USBL system is the depth measurement. It is also apparent that angle uncertainties (depression angle uncertainty especially) were the dominant factor in overall positional uncertainty. The minimum measurement uncertainty was found to be on the order of $u_T \cong 0.2m$.

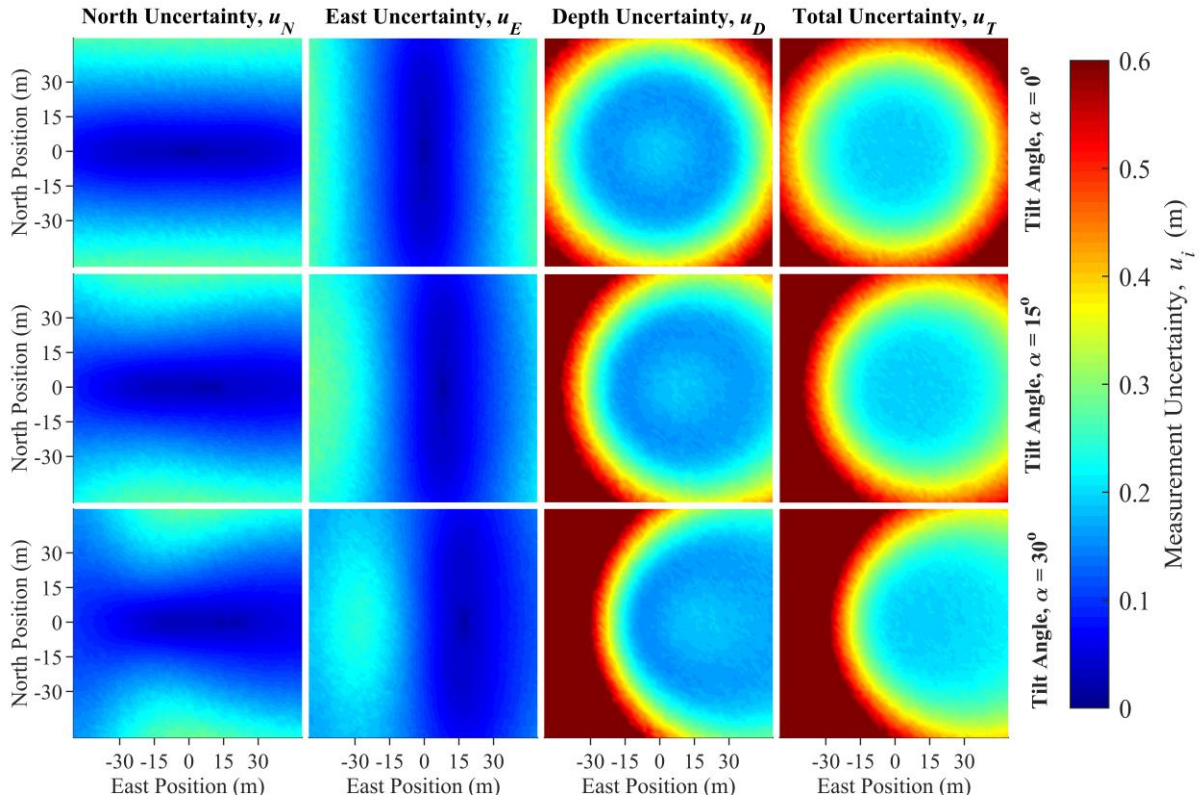


Figure 3.4: Measurement uncertainty heatmaps for fixed-depth, Monte Carlo simulations of USBL configurations with zero transceiver tilt (Top Row), 15° transceiver tilt (Middle Row), and 30° transceiver tilt (Bottom Row). All plots are N - E slices at a depth of $D=10m$. The three left columns show positional uncertainties in the North, East, and depth directions from left to right. The right columns show the total positional uncertainty.

3.1.2. Results in Global Reference Frame

The global reference frame Monte Carlo simulations were performed at fixed-North, $N=0m$, the same region shown in Figure 3.2. Figure 3.4 shows the USBL system uncertainty when USBL transceiver pitch, roll, and heading uncertainty is considered. The values used in this analysis were: $\omega_\phi \sim (0, \sigma_\phi^2)$, $\omega_\theta \sim (0, \sigma_\theta^2)$, $\omega_{\phi,Ship} \sim (0, \sigma_{\phi,Ship}^2)$ where $S_f = 0.25^\circ$, $S_q = 0.25^\circ$, $S_{y,Ship} = 0.30^\circ$. The lowest uncertainty is $u_T \cong 0.2m$, which matches the lowest uncertainty found in Figure 3.2, but in Figure 3.5, the size of that region is significantly smaller. This uncertainty region is approximately 20 meters in diameter. This indicates that the pitch, roll, and heading measurement errors do greatly affect the total uncertainty of the USBL measurement, decreasing the maximum depth that maintains a total uncertainty, $u_T \cong 0.2m$. Additionally, the region of uncertainty $u_T \leq 0.5m$ is more spherical than conical. This was found to be most greatly influenced by the uncertainty in pitch and roll.

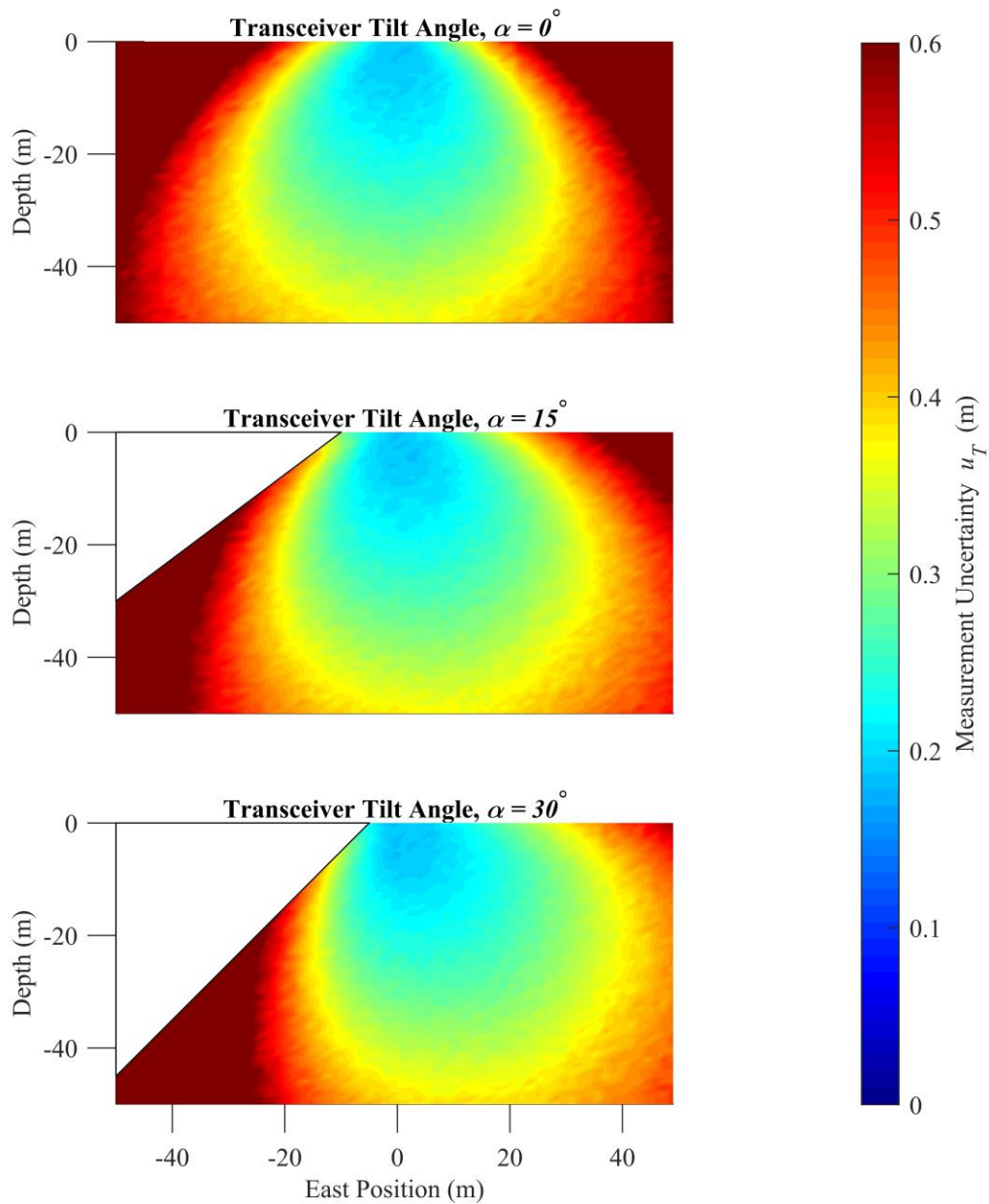


Figure 3.5: Measurement uncertainty heatmaps for $N=0$ fixed-north USBL configurations of zero tilt (Top), 15° tilt (Middle), 30° tilt (Bottom). This includes measurement uncertainty from the surface ship pitch, roll and heading measurements. The white areas are regions outside the range of the uncertainty modeling.

Figure 3.6 is the result of a Monte Carlo simulation that included the ship pitch, roll, and heading uncertainties as well as the ship GPS uncertainty. The GPS uncertainty used was: $\omega_{GPS} \sim (0, \sigma_{GPS}^2)$, where $\sigma_{GPS} = 0.30m$. The lowest uncertainty observed was

$u_T \cong 0.37m$, which is significantly larger than the minimum uncertainty observed in the previous study. Also, the shape of the uncertainty mapping is similar to that of Figure 3.4, suggesting that the GPS uncertainty has much greater effect on the uncertainty magnitude than the uncertainty mapping shape.

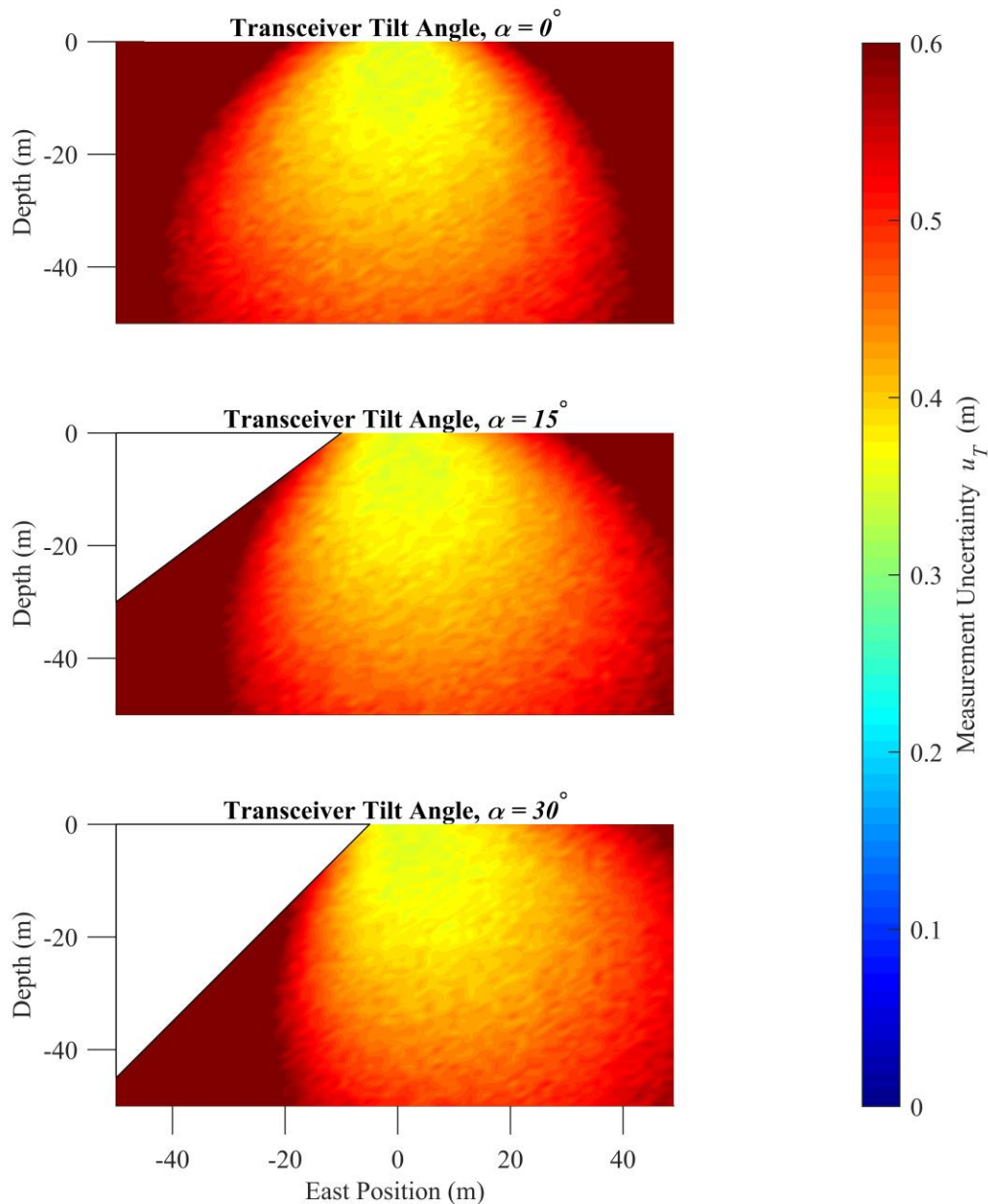


Figure 3.6: Measurement uncertainty heatmaps for $N=0$ fixed-north USBL configurations of zero tilt (Top), 15° tilt (Middle), 30° tilt (Bottom). This includes measurement uncertainty from the surface ship pitch, roll and heading measurements as well as the ship GPS uncertainty.

Figure 3.7 shows the results of the same study in Figure 3.6 but using different sensors as a model. The uncertainty values used in this study were: $\omega_\phi \sim (0, \sigma_\phi^2)$, $\omega_\theta \sim (0, \sigma_\theta^2)$, $\omega_\psi \sim (0, \sigma_\psi^2)$, $\omega_{GPS} \sim (0, \sigma_{GPS}^2)$, where $\sigma_\phi = 0.008^\circ$, $\sigma_\theta = 0.008^\circ$, $\sigma_\psi = 0.08^\circ$, $\sigma_{GPS} = 0.10m$. The lowest uncertainty in Figure 3.7 is $u_T \cong 0.25m$, and the shape of the uncertainty mapping is similar to Figure 3.2. Also, compared Figure 3.4, there is a larger region of $u_T \cong 0.30m$, which would increase the variety of locations the AUV could travel relative to the USBL transceiver. These results suggest that an investment in a highly accurate motion reference unit (MRU) to measure pitch, roll, and heading coupled with an accurate GPS system greatly improves the efficacy of tracking an AUV using USBL.

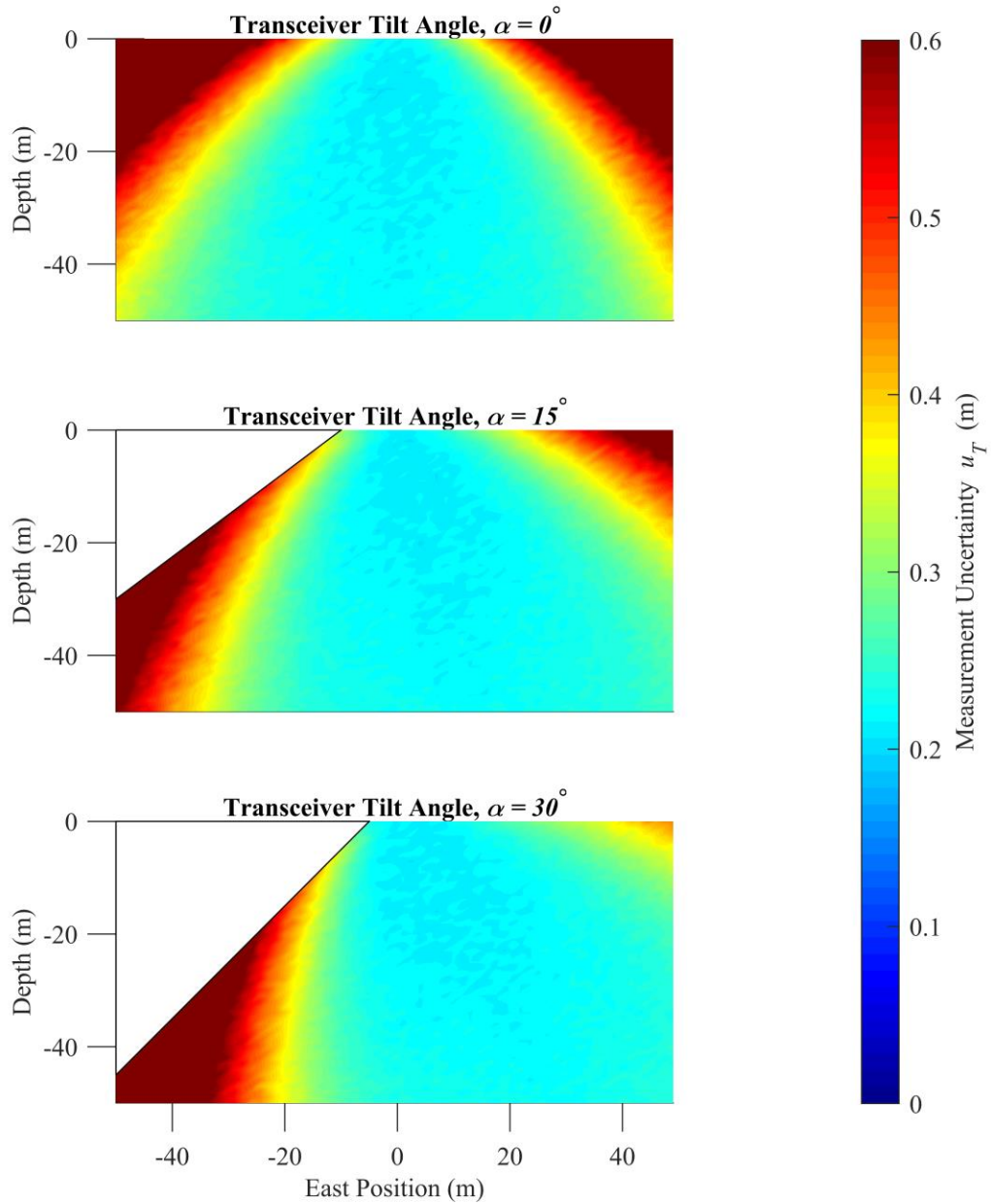


Figure 3.7: Measurement uncertainty heatmaps for $N=0$ fixed-north USBL configurations of zero tilt (Top), 15° tilt (Middle), 30° tilt (Bottom). This includes measurement uncertainty from the surface ship pitch, roll and heading measurements as well as the ship GPS uncertainty using highly accurate, commercially available ship sensors.

3.1.3. Summary of USBL Uncertainty Results

The results shown in sections 3.1.1 and 3.1.2 give information regarding the shape of uncertainty distribution and factors that influence the uncertainty. First, USBL systems have a conic region of highest accuracy; shown in Figures 3.2 and 3.3. Second, USBL measurements of North and East position have a greater accuracy than the USBL measurement of depth. Also, the USBL depth measurement is the greatest contributor to the total positional uncertainty of the USBL system. Finally, Figures 3.5 and 3.6 show that when using a Motion Reference Unit (MRU) and GPS with reasonably accurate measurements of the USBL transceiver position and orientation, the accuracy in the region of lowest uncertainty is approximately $0.35m$. Figure 3.7 shows that by utilizing a more accurate MRU and GPS, this accuracy is reduced to approximately $0.25m$. This large improvement in accuracy shows that the MRU and GPS systems are primary sources of uncertainty in the USBL measurement.

3.2. EKF Results

Each of the EKF cases described in section 2.6 were applied to UI AUV mission data from 2016 field testing [23] to evaluate performance. Additionally, the AUV depth sensor uncertainty, USBL telemetry uncertainty and USBL position uncertainty were included for direct comparison of performance. The USBL uncertainties were determined using the Monte Carlo described in section 2.4 with one modification: rather than solving for all possible AUV positions within a grid, the Monte Carlo simulation was performed for individual AUV positions, based on a one second USBL interrogation interval. These position values were pulled from the onboard EKF log.

Figures 3.8 and 3.9 (zoomed) shows that the post-process filter (*Case 1*, shown in red) matches well with the AUV onboard filter, shown in black. This is seen in the East and North position uncertainty; upper left and upper right plots respectively. This result means the post-process filter performs comparably to the onboard filter and is a valid baseline for investigating the performance of *Cases 2-5*. It is important to note that the *Case 1* filter does not *exactly* match the onboard filter. This is likely due to difference between the data handling of the simulated EKF and the onboard EKF. The onboard EKF handles sensor

measurements in real time, whereas the post-process EKF relies upon recorded time stamps, which may be affected by the data buffer within the AUV hardware. Additionally, in post-processing, the measurements each have different time series due to differences in sampling rates; this requires matching of time series to simulate the EKF, which may introduce slight discrepancies between the simulated and post-processing EKF. Even using the same covariance values, in this application it is difficult to recreate the onboard EKF performance exactly. Despite this difference, the results are still useful for comparison. Figure 3.9 shows the minimum state uncertainty in East and North is approximately 1.3 meters for *Case 1* and 1.1 meters for the onboard filter. Also, both state uncertainty measurements increase at the end of the run, beginning near 250 seconds into the mission. This may be due to ocean currents or the wake of the surface ship the AUV was travelling passed.

Case 2, shown in blue, drops almost immediately to 0.8 meters uncertainty in East position and 0.6 meters in North position. The uncertainty in this filter is highly oscillatory, but it achieves an approximate mean of 0.31 meters of uncertainty in the East position and 0.32 meters of uncertainty in the North position at its lowest value. Additionally, the uncertainty in the East position decreases as the mission progresses but maintains approximately the same magnitude of oscillation. This is possibly due to changes in the USBL East uncertainty, which also decreases over the course of the mission. At 290 seconds into the mission, the USBL East uncertainty drops below the *Case 2* EKF East uncertainty, ending with 0.26 meters and 0.30 meters of uncertainty respectively. The USBL performs better near the mission end due to the AUV travelling within a region of improved USBL East position uncertainty. The North position uncertainty of the USBL system (yellow) is larger throughout the duration of the mission than the *Case 2* EKF (blue). Additionally, the USBL uncertainty gradually increases from approximately 0.36 meters to 0.37 meters between 50 and 100 seconds and then gradually decreases through the end of the mission; the *Case 2* EKF responds similarly. These results suggest that the including the USBL measurements in the EKF reduces the AUV position uncertainty.

Case 3, shown in cyan, behaves similarly to *Case 1* and the onboard EKF, although the uncertainty in the East and North position for case three does fall above the results of the onboard and *Case 1* EKFs. Interestingly, the uncertainty in the depth has a mean of approximately 0.6 meters, while the onboard depth sensor uncertainty is approximately 0.5

meters. This is likely because the EKF includes noise in the measurement and the propagation of the state; the process noise is 0.10859 meters, and the sum of the depth process and measurement noise uncertainty is approximately 0.6 meters. Additionally, the EKF depth uncertainty is significantly smaller than the USBL depth uncertainty, which reaches a minimum value of approximately 3.0 meters at the mission conclusion. The total uncertainty, calculated using equation 2.2, is used to visualize the uncertainty combination of North, East and depth. Figure 3.8 shows that the *Case 3* EKF has a smaller total uncertainty than the USBL until approximately 296 seconds into the mission when the slopes of each intersect. Also note that the USBL total uncertainty has a very similar magnitude to the USBL depth uncertainty. This matches with the results shown in Figure 3.4, where depth is the greatest contributor the total uncertainty in the USBL system. These results suggest that the *Case 3* post-process EKF with the addition of AUV depth performs better than USBL system alone in total uncertainty, despite the superior North and East uncertainty of the USBL.

Case 4, shown in magenta, has little variation from *Case 2* in East and North uncertainty, following the same slope and relative magnitude of oscillations. This is expected, given the only difference between them is the addition of the depth state and measurement in *Case 4*. The EKF depth uncertainty begins near 1.2 meters and decreases to approximately 1.0 meters at the end of the mission. In *Case 4*, depth uncertainty is greater than in *Case 3* for the entire mission. This is likely a result of the magnitude difference between the depth uncertainties of the USBL system and the AUV depth sensor. When the USBL depth measurement is included in the model (*Case 4*), the total uncertainty improves over the baseline AUV depth model (*Case 3*). This suggests that the superior East and North position estimates of the USBL system can benefit the post-process EKF despite the greater uncertainty present in the USBL depth position estimates.

Case 5, shown in green, combines the AUV depth sensor, USBL East and North measurements, and the USBL telemetry-based depth measurement. The resulting East and North uncertainties are greater than previous cases. When adding additional measurements, overall uncertainty should be reduced regardless of the uncertainty of the measurements, but this assumes that the measurements share the same mean, which may not be the case here. The depth uncertainty is significantly improved over *Case 4*, with a mean uncertainty,

$u_D \cong 0.55m$. *Case 5* also has a depth uncertainty slightly lower than that of *Case 3*. It is interesting to note that the uncertainty in the telemetry depth is lower than that of the *Case 5* EKF depth uncertainty. This is likely due to the process noise involved in the depth state propagation as was discussed with the *Case 3* EKF. The total uncertainty of *Case 5* is an improvement over *Case 4*, having a minimum mean total uncertainty, $u_T \cong 0.9m$. The total uncertainty using this EKF scheme is not smaller than USBL total uncertainty calculated using the telemetry depth uncertainty, but this again appears to be a result of the process noise applied to the depth state propagation. Additionally, the implementation of the USBL within the EKF (*Case 5*) allows better handling of poor measurements due to environmental conditions, which improves the confidence in the results.

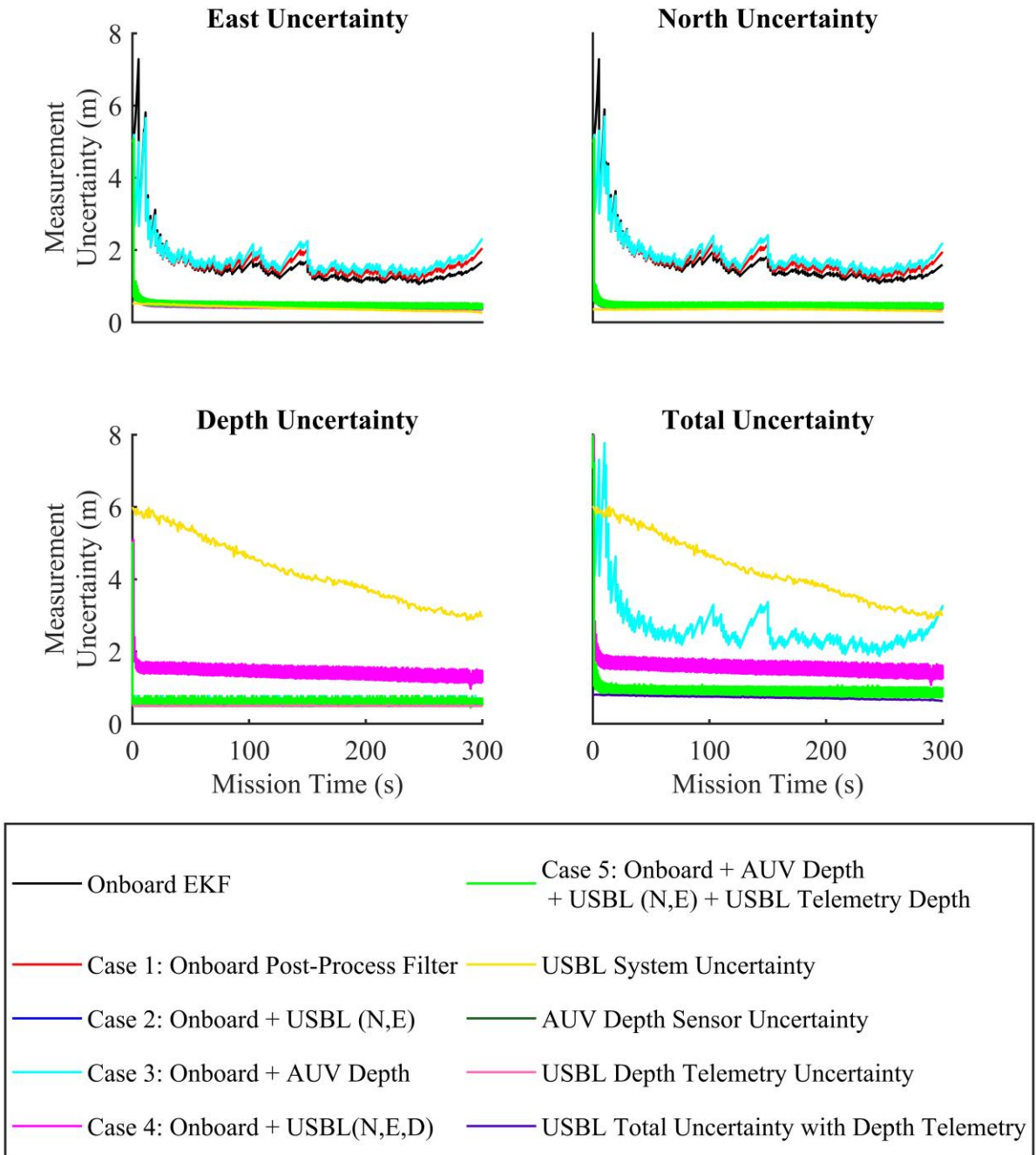


Figure 3.8: The results of the EKF case tests. East position uncertainty (upper left), North position uncertainty (upper right), depth uncertainty (lower left), and total uncertainty (lower right). Additional measurement uncertainties are included for performance evaluation.

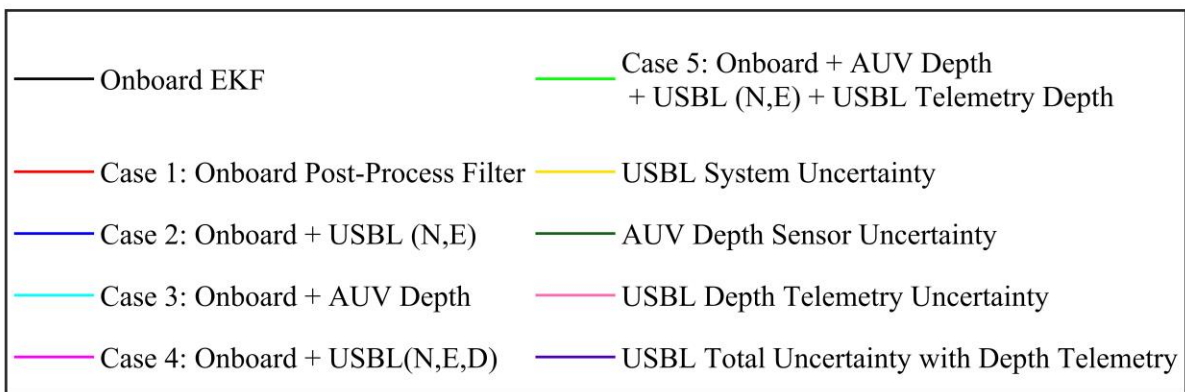
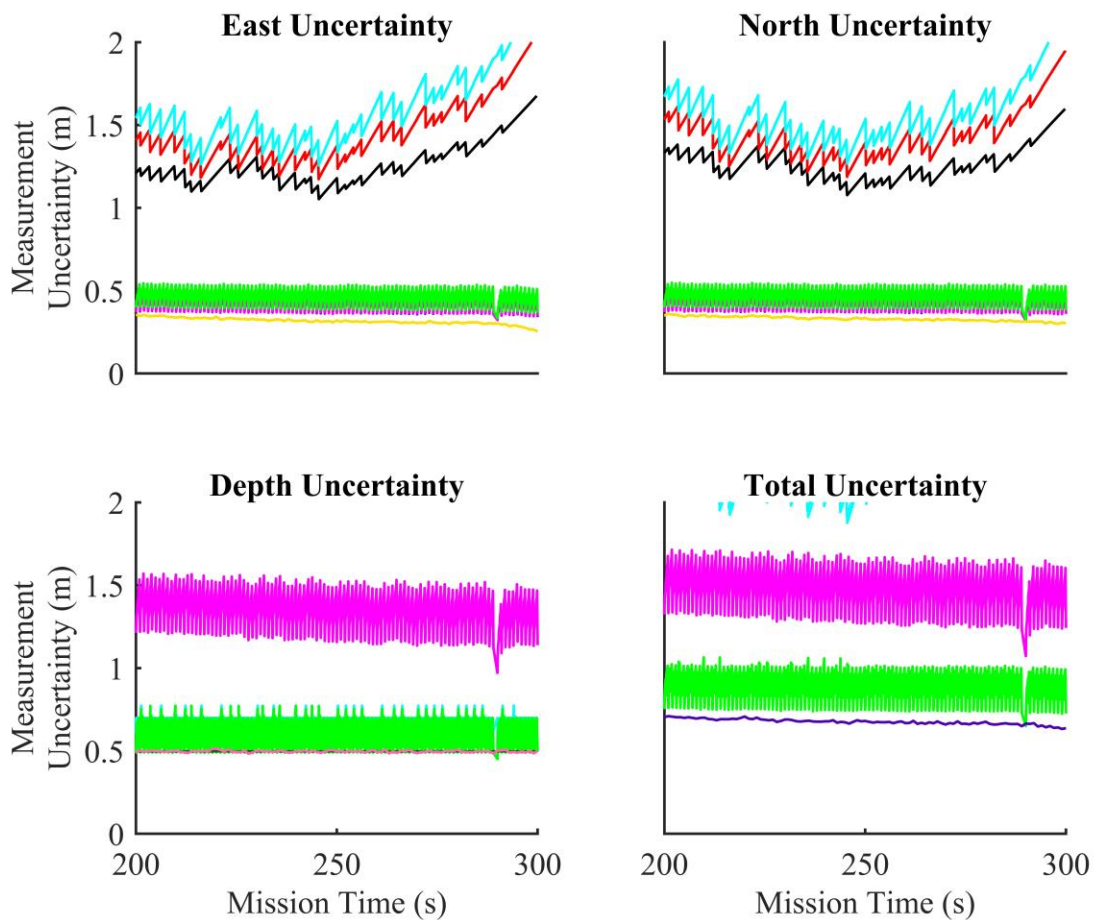


Figure 3.9: The results of the EKF cases, zoomed in to show differentiation between EKF uncertainties.

Chapter 4: Conclusions

The methods and results presented in this research offer an expansion of current AUV localization methods for post-processing research at UI. It has been shown that overall accuracy and uncertainty of AUV localization can be improved utilizing USBL localization integrated with the AUV EKF in post processing. This improvement provides an important benefit to the magnetic and electric field measurements of interest to ONR; with improved localization of the AUV position, the spatial and temporal locations of the magnetic and electric field measurements is known with greater confidence.

4.1. USBL Integration

4.1.1. USBL Monte Carlo Studies

The USBL Monte Carlo simulations were performed using MATLAB to evaluate the spatial dependency of the USBL system measurement uncertainties. The USBL simulation was designed to match commercial USBL system reported accuracies created by a survey of commercially available equipment. The results of USBL uncertainty Monte Carlo simulations, see Figure 3.2-3.6, give evidence that a USBL system could positively influence the localization of the AUV position in the *N-E* plane, but would not greatly benefit AUV depth localization if the AUV is not travelling directly below the USBL transceiver.

Additionally, when considering implementing USBL systems, it is important to be aware that transceiver position and orientation uncertainty can greatly affect the reliability of the USBL position measurements. It was shown that GPS location has the greatest effect on the USBL uncertainty, and an investment in a highly accurate, i.e., $\omega_{GPS} \sim (0, u_{GPS})$, where $u_{GPS} \leq 0.10$ meters, GPS unit for the USBL transceiver would greatly benefit the USBL system localization accuracy. If possible, this research suggests an investment in a quality MRU unit, e.g. the Kongsberg MRU 5+, would also greatly benefit the total uncertainty of the USBL system.

4.1.2. USBL-EKF Integration

The post-process EKF was designed to match the AUV onboard EKF, allowing a direct comparison of the filter performance. The results of this study, shown in Figures 3.8 and 3.9 (zoomed), suggest the inclusion of USBL measurements could greatly improve the localization of UI AUVs during field testing.

The results suggest that immediate benefit could be achieved through the inclusion of USBL East and North measurements to the current AUV EKF. This would perform better than either system independently and applying an EKF would aid the handling of poor acoustic measurements from the USBL. Acoustic measurement error sources include multipathing of the acoustic signal, incorrect sound speed, and acoustic reflections.

Adding depth to the system states did not affect the observability of the system, which allowed for further investigation into tracking AUV depth using the USBL system. The AUV pressure transducer used for depth measurements does outperform the USBL in depth measurements significantly when depth is calculated using the USBL array. Despite the advantage of the AUV depth sensor, the *Case 3 EKF (Post-Process EKF plus AUV Depth)* does not significantly outperform the standalone USBL system. If the USBL North, East, and depth are implemented in an EKF, the total uncertainty is significantly lower than that of the USBL and *Case 3 EKF*. This suggests that the use of the USBL system measurements within the post-processed EKF provides greater benefit to minimizing the total uncertainty than only utilizing AUV and LBL instrumentation.

Given the known difficulty USBL systems have accurately measuring target depth, some manufacturers include a pressure transducer on the USBL transponder and an optional depth telemetry, allowing for a more accurate depth measurement. The results presented in this research suggest that combining the USBL with depth telemetry to the existing UI AUV EKF system could greatly decrease uncertainty in AUV position localization. The USBL system, utilizing depth telemetry, is superior by itself over the *Case 5 EKF*, but combining the USBL with the post-processed EKF (*Case 5*), which includes LBL ranging, is similar in accuracy, but would improve confidence in the accuracy of the state estimates due to the additional independent measurements. It was also found that if the pressure transducer depth measurement can be known more accurately, i.e. utilizing a sensor with a lower uncertainty, the depth and total uncertainty of the case five EKF can be improved.

4.2. Future Work

4.2.1. Field Testing

The UI AUV research team has recently purchased a commercial USBL beacon, which would allow field testing the USBL system. This data could be used to better model the USBL beacon behavior, including improving the uncertainty model for the telemetry uncertainty and the position uncertainty. With further field testing, an integration between the AUV and USBL beacon could be investigated.

This paper studies the utilization of USBL and LBL acoustic localization systems operating concurrently. Acoustic interference between these two systems has not been taken into consideration in this analysis but may be a possible complication. Given that acoustic interference is heavily dependent on the instrumentation and frequency operating range, further field testing is required to determine the effect acoustic interference may have on implementation.

Additionally, the inclusion of a depth state within the AUV onboard EKF has not been implemented. This would require further simulation and field testing to validate. It is imperative to ensure the addition of the depth state would not significantly interfere with AUV navigation during field testing to avoid losing an AUV. The implementation of the depth state would allow full utilization of the USBL system when combined with the AUV EKF.

4.2.2. Rauch-Tung-Striebel Smoother

The Rauch-Tung-Striebel (RTS) smoother [27] is a form of fixed-interval smoother that can be used in conjunction with state estimators, e.g., the EKF, to improve state estimates, typically in post-processing. This smoother utilizes future measurements within the fixed interval to improve the present time estimates, this means that the state at time, $t=k$, can be improved based on state estimates at $t=k+1, k+2, \dots, n$. Utilizing this smoother could improve the state estimates of the AUV when environmental conditions adversely affect the state.

References

- [1] B. Armstrong, E. Wolbrecht, and D. B. Edwards, "AUV navigation in the presence of a magnetic disturbance with an extended Kalman filter," in *Proc. 2010 MTS/IEEE OCEANS Conf. and Exhib.*, Sydney, Australia, 2010, pp. 1–6.
- [2] E. Wolbrecht et al., "Estimating and compensating for water currents: Field testing," in *Proc. 2016 MTS/IEEE OCEANS Conf. and Exhib.*, Monterey, CA, USA, Sep. 19–23, 2016, pp. 1–5.
- [3] E. Wolbrecht et al., "Field testing of moving short-baseline navigation for autonomous underwater vehicles using synchronized acoustic messaging," *The Journal of Field Robotics*, Vol. 30, No. 4, pp. 519–535, 2013.
- [4] L. Paull, S. Saeedi, M. Seto, and H. Li, "AUV navigation and localization: A review," *IEEE Journal of Oceanic Engineering*, Vol. 39, No. 1, pp. 131–149, 2014.
- [5] J. C. Kinsey, R. M. Eustice, and L. L. Whitcomb, "A Survey of underwater vehicle navigation: Recent advances and new challenges," in *Proc. IFAC Conf. Manoeuvring and Control of Marine Craft*, Lisbon, Portugal, Sep. 2006, pp. 1–12.
- [6] P. Milne, *Underwater Acoustic Positioning Systems*, Houston, USA: Gulf Publishing, 1983.
- [7] D. Philip, "An Evaluation of USBL and SBL Acoustic Systems and the Optimisation of Methods of Calibration-Part 1," *Hydrographical Journal*, Vol. 108, April 2003, pp. 18–25.
- [8] B. Bingham, "Predicting the navigation performance of underwater vehicles," in *Proc. IEEE/RSJ Int. Conf. on Intelligent Robots and Systems*, St. Louis, Missouri, Oct. 11–15, 2009.
- [9] P. Batista, C. Silvestre, and P. Oliveira, "GES integrated LBL/USBL navigation system for underwater vehicles," in *Proc. IEEE Conf. on Decision and Control (CDC)*, Maui, Hawaii, Dec. 10–13, 2012.
- [10] P. Batista, C. Silvestre, and P. Oliveira, "GAS tightly coupled LBL/USBL position and velocity filter for underwater vehicles," in *2013 European Control Conf. (ECC)*, 2013, pp. 2982–2987.
- [11] P. Batista, C. Silvestre, and P. Oliveira, "GES tightly coupled attitude estimation based on a LBL/USBL positioning system," in *2013 European Control Conf. (ECC)*, 2013, pp. 2988–2993.

- [12] A. Caiti *et al.*, “Experimental results with a mixed USBL/LBL system for AUV navigation,” in *2014 Underwater Communications and Networking (UComms)*, 2014, pp. 1–4.
- [13] P. X. Song, “Monte Carlo Kalman filter and smoothing for multivariate discrete state space models,” *Can. J. Stat.*, vol. 28, no. 3, pp. 641–652, 2000.
- [14] C. Di Franco, G. Franchino, and M. Marinoni, “Data fusion for relative localization of wireless mobile nodes,” in *Proc. 9th IEEE Int. Symp. on Industrial Embedded Systems (SIES 2014)*, 2014, pp. 58–65.
- [15] Joseph Osborn. “AUV state estimation, navigation, and control in the presence of ocean currents,” M.S. thesis, University of Idaho, 2016.
- [16] D. J. Stilwell, A. S. Gadre, C. A. Sylvester, and C. J. Cannell, “Design elements of a small low-cost autonomous underwater vehicle for field experiments in multi-vehicle coordination,” in *2004 IEEE/OES Autonomous Underwater Vehicles*, 2004, pp. 1–6.
- [17] Jordan Stringfield. “Navigation and localization of an autonomous underwater vehicle fleet for magnetic field measurements,” M.S. thesis, University of Idaho, 2012.
- [18] B. Armstrong *et al.*, “Field measurement of surface ship magnetic signature using multiple AUVs,” in *Proc. 2009 MTS/IEEE OCEANS Conf. and Exhib.*, Biloxi, MS, USA, 2009, pp. 1–9.
- [19] John R Canning, Michael J Anderson, Dean B Edwards, Michael ORourke, Thomas A Bean, Jesse L Pentzer, and Douglas L Odell. “A low bandwidth acoustic communication strategy for supporting collaborative behaviors in a fleet of autonomous underwater vehicles,” in *US Navy Journal of Underwater Acoustics*, 2009.
- [20] Christopher Walker. “Magnetic signature mapping of a moving ship using a fleet of autonomous underwater vehicles,” M.S. thesis, University of Idaho, 2012.
- [21] David Schipf, John Feusi, Matthew Anderson, Eric Wolbrecht, John Canning, and Doug Edwards. “Using AUV-acquired survey data to derive a magnetic model for a surface vessel,” in *Proc. 2013 MTS/IEEE OCEANS Conf. and Exhib.*, San Diego, CA, USA, 2013, pages 1–8.
- [22] S. R. Qualls *et al.*, “Underwater electric potential measurements using AUVs,” in *Proc. 2015 MTS/IEEE OCEANS Conf. and Exhib.*, Washington, DC, USA, 2015, pp. 1–4.
- [23] R. Ross *et al.*, “Underwater Electric Field Measurement and Analysis,” in *Proc. 2017 MTS/IEEE OCEANS Conf. and Exhib.*, Anchorage, AK, USA, 2017, pp. 1-5.

- [24] D. C. Handscomb and J. M. Hammersley, *Monte Carlo methods*, London: Methuen, New York, USA: Wiley, 1964.
- [25] L. E. Kinsler, A. R. Frey, A. B. Coppens, and J. V. Sanders, *Fundamentals of Acoustics*, 4th ed. Hoboken, USA: Wiley, 1999.
- [26] R. M. Eustice, H. Singh, and L. L. Whitcomb, "Synchronous-clock, one-way-travel-time acoustic navigation for underwater vehicles," in *The Journal of Field Robotics*, Vol. 28, No. 1, pp. 121–136, Jan. 2011.
- [27] D. Simon, *Optimal state estimation: Kalman, H [infinity] and nonlinear approaches*, Hoboken, USA: Wiley-Interscience, 2006.